Sub-arctic river bank dynamics and driving processes during the open-channel flow period

Lotsari E.[1,2*], Hackney C.[3], Salmela J.[2], Kasvi E.[2], Kemp J.[4], Alho P.[2,5], Darby S.E.[6]

[1] Department of Geographical and Historical Studies, University of Eastern Finland, Yliopistokatu 2, P.O. Box 111, 80101 Joensuu, Finland

[2] Department of Geography and Geology, University of Turku, 20014 Turun yliopisto, Turku, Finland

[3] Energy and Environment Institute, University of Hull, Cottingham Road, HU6 7RX, Hull, UK.

[4] Australian Rivers Institute, Griffith University, Nathan, Qld Australia 4111

[5] Finnish Geospatial Research Institute, National Land Survey of Finland, Geodeetinrinne 2, 02430 Masala, Finland

[6] School of Geography and Environmental Sciences, University of Southampton, Highfield, Southampton, SO17 1BJ, UK.

*corresponding author: e-mail: eliisa.lotsari@uef.fi, tel: +358 50-5758297

Data availability statement

Research data are not shared.

Abstract

There is growing concern that rapidly changing climate in high latitudes may generate significant geomorphological changes that could mobilise floodplain sediments and carbon; however detailed investigations into the bank erosion process regimes of high latitude rivers remain lacking. Here we employ a combination of thermal and RGB colour time-lapse photos in concert with water level, flow characteristics, bank sediment moisture and temperature, and topographical data to analyse river bank dynamics during the open-channel flow period (the period from the rise of the spring snowmelt flood until the autumn low flow period) for a subarctic river in northern

Finland (Pulmanki River). We show how variations of bank sediment temperature and moisture affect bank erosion rates and locations, how bank collapses relate to fluvial processes, and elucidate the seasonal variations and interlinkages between the different driving processes.

We find that areas with high levels of groundwater content and loose sand layers were the most prone areas for bank erosion. Groundwater seeping caused continuous erosion throughout the study period, whereas erosion by flowing river water occurred during the peak of snowmelt flood. However, erosion also occurred during the falling phase of the spring flood, mainly due to mass failures. The rising phase of the spring flood therefore did not affect the river bank as much as its peak or receding phases. This is explained because the bank is resistant to erosion due to the prevalence of still frozen and drier sediments at the beginning of the spring flood. Overall, most bank erosion and deposition occurrences were observed during the low flow period after the spring flood. This highlights that spring melt, while often delivering the highest discharges, may not be the main driver of bank erosion in sub-arctic meandering rivers.

Keywords:

river bank dynamics; fluvial processes; groundwater; mass failures; remote sensing

1. Introduction

Studies examining seasonal variations of sediment transport and its driving agents (e.g., by flowing water, groundwater, and mechanical bank failures) remain limited in high-latitude subarctic rivers, especially in comparison to those undertaken on mid-latitude river systems (Rozo et al. 2014). The channel morphodynamics of subarctic rivers are influenced throughout the year by several key variables in addition to discharge from the contributing catchment. These key variables include: 1) hydro-climatic variations over both annual and seasonal timescales; 2) sub-zero temperatures and the duration of river ice cover; 3) the extent of inundated floodplain as dictated by channel flow and channel-floodplain ice conditions; and, 4) the geotechnical characteristics of river banks, which will be affected by sub-aerial processes (Vandenberghe, 2001; Turcotte et al., 2011; Lewis et al., 2012; Kämäri et al., 2015; Lotsari et al., 2017). Each season exerts different controls on the channel flows, sediment transport, and morphology and these controls may differ also between regions, i.e., at varying temporal and spatial scales, with differing hydro-climatic conditions and varying magnitudes of the season specific processes (Tananaev, 2016).

The role of high discharge events on the erosion and deposition of river channels has been the subject of debate. Even for the more frequently studied case of mid-latitude rivers there is no clear consensus on the efficacy of high flows, with studies illustrating that site specific conditions determine whether erosion is dominantly associated with peak flows (Hooke, 1979), or otherwise (Baker, 1988). In cold environments, the spring snowmelt is generally considered to transport the largest volume of sediment in a single event; however, the low flow seasons and river ice itself may cause the greatest overall channel changes and highest amounts of sand/gravel transport (Lotsari et al., 2014a and 2015).

The current body of research on subarctic rivers lacks detailed descriptions of the processes responsible for erosion of the channel boundaries. Without understanding in detail how seasonally varying sub-aerial (i.e. freezing/thawing, rain, groundwater seepage) and fluvial entrainment processes affect river dynamics, it is impossible to assess the long-term impacts of hydro-climatic variations on flooding, bank collapse and sediment transport further downstream. Improved understanding of these complex and interacting processes are needed, as lateral river bank erosion, which is affected by both fluvial and sub-aerial processes, can deliver a substantial proportion of the total sediment yield reaching the oceans (Milliman & Meade, 1983; Walling, 2005; Walling & Collins, 2005; Kronvang et al., 2012; Leyland et al., 2017).

The origin (e.g., channel bed or bank) of seasonally exported sediment from subarctic and high-altitude river systems needs to be quantified, particularly given the lack of understanding of how banks respond to changing water levels and freezing/thawing conditions. Impacts of freezing and thawing on bank erosion generally have mainly been examined in an engineering context (Wang et al., 2008; Guo & Shan, 2011; Hazirbaba et al., 2011; Ling et al., 2015; Qian et al., 2015), but limited information is available for subarctic rivers, in which frozen ground can limit sediment supply from the catchment and the river channel during spring flows, but erodibility may be enhanced during the summer and autumn low flow periods (Tananaev, 2013). Therefore, it is important to examine the relationships between geotechnical properties and lateral channel erosion to understand the feedbacks operating between processes in seasonally frozen environments (Rinaldi & Darby, 2008).

Combined analyses of the influence of all relevant processes, including the role of fluvial erosion, the impacts of rain and groundwater, and bank stability with respect to gravitational failure, would enable a fuller understanding of feedback systems between processes acting on river banks (Rinaldi & Darby, 2008). For example, in a study of The Brahmaputra River (26 ° 50 ′ 08 ″ N latitude) with composite banks, Karmaker and

Dutta (2013) found that the total annual bank erosion was controlled by the combination of groundwater seepage and fluvial erosion. Fox et al. (2007) also showed, in a small mid-latitude headwater river of the Mississippi River, that the impacts of groundwater seepage can be significant for bank collapses. They found that erosion was caused by the combined processes of reduced cohesion due to saturation of bank material and overland erosion from the discharging seep. Fox et al. (2007) showed that the low flow seeps, which occur during summer rain events, act in conjunction with overland flow and fluvial entrainment to promote bank instability. However, in subarctic rivers, groundwater seepage has been studied only in the context of understanding the impacts of water temperature variation on fish ecology (Dugdale et al., 2018), and not in terms of their potential effects on river bank erosion.

Recent technological advances in the measurements of flow characteristics, sediment transport, topography and thermal properties of the river channels offer fresh potential for detecting fluvial and sub-aerial processes at increased spatial and temporal resolution, as compared to traditional measurement techniques (Rennie et al., 2002; Demers et al., 2011 & 2013; Vaaja et al., 2011; Westoby et al., 2012; Dugdale et al., 2013; Brasington et al., 2016; Burtin et al. 2016; Kasvi et al., 2017). For detecting the melting of soil/sub-surface water in subarctic systems, thermal imaging and associated soil/bank sediment moisture and temperature observations can reveal the impacts of temperature variations on river channel erosion. Lawler (2008) has argued that bank thermal dynamics and light intensity patterns can index geomorphologically-important processes, with the use of continuous thermal data showing that river banks are highly dynamic thermally and respond quickly to radiation inputs. To our knowledge, there have been no studies which have applied thermal imaging for detecting bank erosion processes in subarctic meandering rivers.

Moreover, there is great potential to combine such thermal imagery data with normal RGB colour time-lapse photos and detailed geotechnical, river flow (e.g. Acoustic Doppler Current Profiler, ADCP), and seasonal topographic change data (e.g. terrestrial laser scanning, TLS; Neugirg et al., 2016; Leyland et al., 2015 and 2017; Williams et al., 2018), so as to detect whether seasonal bank erosion relates to the areas of the greatest temperature variation, groundwater seepage, or changes in ice/freezing conditions. In short, temporally dense measurements have the potential to reveal when, where and why channel banks are retreating.

This study aims to analyse the driving processes of the river bank dynamics during the open-channel flow period, i.e. from the rise of a spring snowmelt flood until the autumn low flow period, capturing for the first time the relative impacts of variation in bank sediment temperature and moisture, temporal water level fluctuations, and seasonal variations and interlinkages between the different driving processes.

2. Study site

The meandering Pulmanki River is a tributary of the Tana River in northern Finland and has a catchment area of 484 km^2. The study area is located along the channel 3.5 km (2 km if straight distance) upstream of Lake Pulmanki (Fig. 1). The Pulmanki River is unregulated and freezes up to seven months of the year. Its hydrological regime is subarctic-nival in that the largest peak flows are generated by snowmelt and the break-up of river ice (Lininger and Wohl, 2019; Woo and Thorne 2003). Smaller discharge peaks are associated with rain events during summer.

The region was deeply glaciated under the Fennoscandian ice sheet in the Late Weichselian, which reached a local maximum in northern Finland at 21 ka. This was followed by retreat and a subsequent re-advance between 11.6 and 12.7 ka, when the region lay near the outer limits of the Younger Dryas ice sheet (Svendsen et al., 2004; Stroeven et al., 2016). During the final wasting of the ice sheet, an ice-dammed lake occupied the terminal Pulmanki River valley (Johansson, 1995 and 2007). A valley fill of glacio-lacustrine and glacio-fluvial sediments along the lower Pulmanki was deposited after the lake drained (Hirvas, 1988). River incision into these unconsolidated deposits is evident for tens of kilometres upstream of the present-day Lake Pulmanki.

Active migration in the meandering river upstream from Lake Pulmanki is c. 0.2–1 m yr^{-1}, and bank protection measures have been installed on some bends downstream from the study reach (Lotsari et al., 2014b). Here, we concentrate on a single cut bank on one meander bend. The study bank is 13–18 m high and comprises 1.5–16 m loose, very well sorted fluvial sand with weak soil development in the upper 0.3 m, with additional cohesion provided by the root mass above 0.5 m depth (Fig. 2). This overlies 15 m of laminated fine sandy silt and, clayey siltassociated with the proglacial Lake Pulmanki. This lacustrine unit is obscured in some places by weakly cemented, <0.5 m fine-textured talus derived from the overlying lacustrine unit. The bank stratigraphy is therefore complex, with cohesive silts underlying non-cohesive sand, in a reversal of the usual “composite” structure along parts of the bank exposure.

The wavelength of the bend is 301 m with a thalweg length of c. 390 m, giving a local sinuosity of 1.3. The width of the channel at low flow (i.e. the channel bed) at the apex is 20 m and the bankfull width is 36 m (Lotsari et al., 2014b). The bend can be classified as a compound bend and it is asymmetric. Typically the highest rates of erosion occur in the downstream part of the bend, i.e. at the second apex of the compound bend, which is the main interest area in this study (Fig. 1 and Lotsari et al.

2014b). The bank surface angle was calculated from topographical data as 36º at the apex.

Fig. 1.

Fig. 2.

3. Data and methods

This study is based on measurements undertaken during 2017. The analyses are based on the FLIR (Forward Looking Infra-Red) camera and normal RGB colour time-lapse camera photos, in addition to water level, bank sediment moisture and temperature, river flow characteristics (ADCP) and topographical data (TLS) (Table 1). Additional sedimentary data had been collected during 2012–16 (see sections below).

Table 1.

3.1. Laser scanning

The bank was scanned with a Riegl VZ-400 TLS over an eight day period in spring 2017 and for two days in autumn 2017 (Table 1). The spring 2017 scans took place daily, encompassing the period before and during the rising phase of the snowmelt flood (Table 2). The autumn 2017 scanner data captured the end of the ice-free flow period, before freezing of the river. The TLS was located on the inner-bank point bar on the left side of the river, for scanning the high outer bank of the right side of the channel. The scan was done once a day (panorama 10 setting: 2 cm point spacing at 100 m distance). For the purpose of assessing accuracy, scanning was performed twice on 5.6.2017, with two different set ups (panorama 10, and also panorama 20: 4

cm point spacing at 100 m distance). In both of these scans, the targets and scanner were in exactly the same location, and identical RTK-GNSS measurements of the targets were also applied. The difference in the two scans therefore enabled the level of detection due to the scanner itself to be calculated.

The data was georeferenced using targets whose locations were measured with the RTK-GNSS (real-time kinematic - global navigation satellite system) (Table 2). The targets were placed on both sides of the channel (Fig. 1). During all of the measurements, the same number of targets were deployed. However, in the final georeferencing, only those targets, which resulted in the best georeferencing result, were used (Table 2). To assess the accuracy of the georeferenced point cloud of each measurement time step, the standard deviation between the RTK-GNSS measurements of the targets and the georeferenced point cloud was calculated (Table 2).

Table 2.

During the georeferencing process, the point clouds were also filtered as follows: 1) the bank was delineated from the point cloud, 2) every 3rd point was selected (point filter), 3) Easily detectable vegetation (e.g., isolated grass patches and trees on top of the bank) returns were deleted manually, 4) reflections from water surface were deleted based on the known water elevation (height filter), 5) the land cover was selected by filtering the vegetation out from the data (terrain filter), 6) octree filtering was applied to select equal interval points every 5 cm. This point spacing was selected to reduce the overall size of the data set, and it was still showing the small-scale topographical variation. As a result, cleaned point clouds were gained, which included only the bank surface topography.

Bank topography changes (DEMs of difference: DoD) and their locations were analysed in CloudCompare software using the Multiscale Model to Model Cloud Comparison (M3C2) distance analyses plug-in (Lague et al., 2013). The results were exported to ArcGIS for further analysis of the erosion and deposition locations. These bank changes were detected for the spring (30.5.-6.6.2017: daily), the whole summer (6.6.-6.9.2017), and the autumn (6.-8.9.2017) periods.

The Level of Detection (LoD) was calculated based on the standard deviations presented in Table 2, as no other reference data were available. The 68 % confidence limit was calculated as:

$$1 * \sqrt{\sigma_1^2 + \sigma_2^2} \quad (1)$$

where σ_1 is the standard deviation of the TLS georeferencing error of the initial scan and σ_2 is the standard deviation of the TLS georeferencing error of the subsequent scan (see values from Table 2). The 95 % confidence limit was calculated following Milan et al. (2007) as:

$$1.96 * \sqrt{\sigma_1^2 + \sigma_2^2} \quad (2)$$

The scanner's accuracy was revealed from the analyses done between scanning 1 (S1) 1 and scanning 2 (S2) of 5.6.2017. The 95 % confidence limit between two consecutive scans on 5.6.2017 using the same scanner position and targets was 0.017 m (Table 3). Thus, this is the LoD due to the scanner itself.

Table 3.

Daily topographical changes were analysed in spring, i.e. before and during the rising phase of the snowmelt discharge event. The topographical change was also analysed between the first and last measurement of the spring field campaign, between the last measurement of the spring and the first measurement of the autumn field campaign, and between the two measurements of the autumn period. The analyses between the two days in the autumn low flow period were done to reveal if any bank collapses occur during stationary weather and water level conditions. The distances between two point clouds and the volumetric changes were calculated using the M3C2 tool (Lague et al., 2013). As a result of the analyses, significant change values were also obtained. These represent a distance larger (at the 95 % confidence interval) than a measure of the roughness of the river bank and point density (Lague et al., 2013).

3.2. Bank sediment moisture and temperature

Bank sediment moisture and temperature sensors (i.e., Onset HOBO microstation data logger with two moisture probes and two temperature probes) were deployed in four different locations across the bank profile to enable the detection of variations in moisture and groundwater. One sensor was located in the clay toe area (location a, cf. Fig. 1, Table 4). The second was located in the lower bank in the “slightly gravelly sand” layers (location b). The third location was higher up in the “gravelly sand” layers (location c). The fourth sensor was located in the top soil layer (location d). This layer was still frozen in late May 2017 and it was not possible to install the sensors very deeply (Table 4). Note that there was no snow at these locations during the installation. In each of these four locations, two moisture and two temperature probes were attached to one HOBO data logger. These probes were at two different elevations in each sensor location (Table 4).

Table 4.

3.3. Sedimentary data

Sediment samples were collected in 2017 from two of the HOBO locations (locations b and c: Fig. 1, Table 4). Sediment samples from the bank surface were also collected in autumn 2012 (Fig. 1, Appendix 1). In addition, the bulk density was analysed based on samples taken on 22.5.2016 (Fig. 1, Table 6). All of the samples were also dry sieved and their particle characteristics described. The critical bed shear stresses of the toe area samples were estimated based on their D_{50} values using Julien (2002).

The cohesion and friction angle of the bank materials were determined using an Iowa Borehole Shear Tester (BST) deployed in September 2015 (Fig. 1), following Darby (2005) and Lutenegger and Hallberg (1981). Sediment samples extracted from the BST measurement locations were also analysed to determine the D_{50} and the overall silt and clay content of the tested materials.

3.4. FLIR and RGB colour photos

The FLIR photos (taken on a FLIR 640 Vue Pro camera: 7.5-13.5 µm spectral band, 13 mm lense, 640 resolution, 45° FOV, 9 Hz) revealed the spatial and temporal variation (relative variation, not actual temperature values in the pixels) of the thermal and moisture characteristics of the river bank during the rising stage of the flood

(30.5.–6.6.2017) and during the autumn (6.-8.9.2017) period. FLIR photos were taken every minute throughout the measurement periods. Morning hours were missing due to poor battery performance. The FLIR camera was mounted to film the most erodible downstream part of the bank, where bank composition varies vertically along the bank together with apparently moister and drier areas (Table 1, Fig. 1). The FLIR photos also covered the HOBO sensor locations.

The camera calibrated itself before each photo. The photos captured the spatial and temporal variation of the relative heat of the bank during the day and night. The bank's surface heat variation was detected and visually compared to the topographical change locations calculated from the TLS data.

The standard RGB colour photos were taken with two time-lapse cameras (Burrell game cameras: Focus length 6mm; Sensor size 1/3 inches; Pixel Pitch 3 MP), which were installed in February 2017 next to the FLIR camera location. Cam1 filmed the bank apex area, and cam2 filmed the inlet area of the sub-bend in question. These two cameras filmed the erosion-prone bank every two hours. The occurrence of erosion and deposition in the toe and top sections of the bank were detected throughout the open-channel period based on these photos. Visual interpretation enabled us to classify the erosion and deposition magnitudes as either "great" (class 0.2) or "small" (class 0.1). Note that these class names are qualitative descriptors, and were defined in a numerical format for visualization purposes (cf. Fig. 3). These occurrences were compared to the driving agents revealed from the other data sets (see below). Videos were made from the time-lapse photos from the time period, which both cameras covered (i.e. 30.5.2017–30.6.2017). The time-lapse camera1 had ceased functioning already at 1.7.2017, but cam2 functioned throughout the whole measurement period until September 2017 (Fig. 3). The videos are available in the supplementary material for this paper.

3.5. Flow characteristics

A Sontek M9 ADCP sensor (moving kayak platform) was deployed to measure flow velocity, direction and depth next to the bank (cf. Table 1 for measurement times). A standard moving-platform setup was used with readings taken at frequency of 1 Hz. Discharge was also captured in cross-section transects on 31.5., 5.6., 6.6. and 7.9.2017. In addition, a RQ-30 (Sommer) sensor located c. 1.2 km (straight length) downstream from the studied bank. It measured the discharge every 15 minutes throughout the study period (Table 1).

Post-processing was conducted in RiverSurveyor Live and Matlab. For shear stress calculations, data was smoothed over two ensemble widths (~50 cm) to smooth peaks. Boundary shear stresses were derived from the velocity gradient, *m,* calculated using a least-squares regression between *ln(z)* and *u*, where *u* is the velocity at elevation *z* above the bed, for each vertical ensemble within the ADCP transect. The shear velocity, $u*$, was calculated as:

$$u_* = \kappa m \tag{3}$$

where κ is the von Karman constant of 0.41, and the boundary shear stress, τ, was calculated as:

$$\tau = \rho u*^2 \quad (4)$$

where ρ is the density of water (kg/m^3). All regressions exclude data in the lower 6% of the flow where acoustic sidelobe interference affects the accuracy of the ADCP-acquired velocity estimates. As such, the ADCP does not record data in the bottom 6% of the channel. The highest erosional forces observed were compared against measured erosion and critical shear stresses derived from sediment samples (ranging from 0.004 to 0.529 n M^{-2} for the grain size range of 0.004 mm to 0.53 mm observed; Julien, 2002) to detect whether the flow forces could potentially have caused the observed erosion.

Water level was measured with the RTK-GNSS at the locations of the installed Solinst Levelogger pressure sensors. Those were at the upstream part of the studied bend, and in one meander bend c. 1.5 km (straight length) downstream of the bank. The variation of the water level was gained from these locations throughout the study period.

4. Results

4.1. Water level and flow characteristics

In addition to reporting the flow variations, it was detected whether these variations lead to events that exceed incipient motion thresholds. Even though the river ice had broken up on 5.5.2017, based on time lapse RGB photos, the snowmelt discharge peak of 72 m^3/s occurred on 9.6.2017. Spring of 2017 was unusually cold and the flood peak was later than usual, and the initiation of the snowmelt discharge flood was slow. The first discharge measurement, undertaken on 31.5.2017 was 9.4 m^3/s (water surface elevation of 15.4 m.a.s.l.). The stage started to rise on 3.6.2017 and the flood, mainly caused by snowmelt, lasted until 19.6.2017. The spring flood had two peaks. The first occurred at 4:45 am on 9.6.2017 and had a water level of 17.47 m.a.s.l. (Fig. 2). The water level had gone down to 17.22 m.a.s.l. on 9.6.2019 at 7:00 pm, and risen again to 17.53 m.a.s.l. at 6:15 am on 10.6.2017, when the second peak of the spring flood occurred.

The first discharge event, solely caused by rain, was during 19–21.6. (Fig. 3: WL and d sensor). Note that on 21.6., the point bar on the inner bend emerged above water for the first time after the initiation of the spring snowmelt flood. During May-June 2017, varying weather conditions, consisting of heavy rain, snow, hail and temperatures from -4 to +21 ^{o}C, were noted in addition to the rising water level (Fig. 3). The summer was also very wet and there were multiple discharge peaks due to rain.

Fig. 3.

Overall, mean velocities remained fairly constant between the two survey periods. Mean velocity in autumn was 0.28 m/s compared to 0.31 m/s in spring. However, the bed shear stress was greater in the autumn next to the bank (Fig. 4), partly due to the shallower depth (mean depth 0.54 m in autumn compared to 0.88 m in spring), and the fact that the measurements were taken closer to the bank toe during the spring.

Fig. 4.

At all flows, bed shear stresses exceeded the maximum critical shear stress (0.529 N/m^2; Julien, 2002) of the D_{50} grainsize at multiple locations along the ADCP transect

(Figs. 1, 4 and 5). As such, bed shear was able to induce erosion during both spring and autumn flow regimes. Thus, the shear forces of flowing water are large enough to move sediment throughout the open channel flow period.

4.2. Sedimentary characteristics of the bank

Based on the borehole shear tests performed in 2015, the bank material in the toe area around the apex (BST2) has a friction angle of 36.5°, and 35.0° at the top of the bank (BST1) (Fig. 1, Table 5). The bulk densities were 1.43–1.73 g/cm^3 and less than 12 % of the sediments consisted of silt and clay (Tables 5 and 6). When compared to the actual bank surface angle (36° at the apex), the bank proved to be very prone to mass failures.

Table 5.

Table 6.

4.3. The topographical changes of the bank based on laser scanning and time-lapse photos

Morphological changes observed across the outer bank are presented in Tables 7–9 and Fig. 5. When the longer periods were detected, the 6.6.2017–6.9.2017 period had the greatest average significance value (i.e. 0.92 m), next was the spring period 30.5.2017–6.6.2017, and the smallest significance value occurred during the autumn steady flow period of 6.9.2017-8.9.2017.

Due to the greatest LoD value of 6.2 cm, the distances (i.e. changes) within +/- 6 cm were defined into the “no change” category, and visualized using grey in Fig. 5. The topographical changes of the rising phase of the spring snowmelt discharge event (30.5.2017-6.6.2017) overall were smaller based on the TLS data than of the rest of the measured open channel flow period (6.6.2017-6.9.2017). However, greater changes occurred in certain locations: there was erosion in the toe area of up to 0.16 (location 1) and 0.28 m (location 5), and there was 0.32–0.46 m (locations 3 and 4) maximum erosion observed in a gully area higher within the bank (Fig. 5, Table 8). However, spatially, there was more deposition than erosion, and deposition areas of c. 0.40 m (location 4) also occurred.

Fig. 5.

During the summer, i.e. when comparing the spring (6.6.2017) and autumn (6.9.2017) TLS data, the greatest erosion (c. 0.65 m) occurred in the toe area at the downstream part of the channel (Fig. 5 and Table 8: location 2). In addition, continuous toe erosion occurred at location 5, in the area of the looser sand layers (Figs. 5–6, Table 8, the supplementary video material). More than 0.6 m of erosion and deposition occurred in the downstream part of the channel, slightly higher up in the bank (location 1). Unfortunately, this change was not captured in the time-lapse cameras, as the area was outside of the camera's view. Thus, we do not know the exact time when mass failure at this location happened during the 6.6.2017-6.9.2017 summer period. It had not occurred during the spring field campaign of 30.5.2017-6.6.2017.

Table 7.

In autumn, very few changes occurred. However, 0.07–0.14 m erosion occurred at locations 3-5 (Fig. 5 and Table 8). These change locations were not as distinct as in the other analysed periods. During this autumn measurement period there were no major weather or water level changes, thus the only cause can be mass failures due to gravity, or groundwater seepage.

Table 8.

Table 9.

The frequencies of the channel changes in the rising, peak flow and falling phases of the spring flood (Figs. 3, 5 and 6, and supplementary material) were also analysed. The analyses, based on the time-lapse RGB photos, revealed that toe erosion caused by flowing river water occurred most frequently during the snowmelt discharge event peak within 2 days (cam1, apex area: 17 times; cam2, inlet area: 7 times), and during the falling stage within 9 days (cam1: 38 times; cam2: 42 times), mostly due to mass failures. These changes were thus faster, than during the rising flood stages (cam1: 17 times; cam2: 7 times), which lasted 8 days and when the ground was frozen. Toe deposition was the greatest during the 9 day long falling phase of the spring flood (cam1: 51 times; cam2: 33 times). During the peak of the snowmelt discharge event, there was mostly toe erosion and the material was transported away by river flow directly after slumping.

When analysing the spatial locations of the toe erosion events, the bank can be divided into the inlet and apex areas (based on cam1 and cam 2, Fig. 6). The fluvial toe erosion was faster around the apex of the bend during the rising and peak phases of the spring discharge event, as compared to the upstream inlet area. However, after the peak of the flood, toe erosion became more frequent in the upstream inlet part of the bend than at the apex. Thus, the focus of greatest erosion changed location over time.

The frequencies of erosion events during the spring flood event (30.5.2017-19.6.2017) were also compared to the rest of the open-channel flow period (20.6.2017-6.9.2017) (Figs. 3 and 6). The cam2 revealed that the total number of toe erosion (cam2: 97 times), toe deposition (cam2: 89 times) and top erosion (cam2: 42 times) occurrences were greater during 20.6-6.9.2017 than during the spring snowmelt flood hydrograph. However, these events occurred over a period 100 days, thus they were not as frequent as during the spring flood phases. In autumn, between the 6.9.2017-8.9.2017, only small changes were observed based on TLS data, but these were not quantified in the bank erosion event counts as no time-lapse camera data was available after 6.9.2019.

Fig. 6.

During the receding phase of the spring flood, bank erosion was dominantly effected by shallow planar failures with deposition on the toe as the water table lowered (Figs. 3, 5, 6, and supplementary video material). Some bank toe erosion was also observed in the receding phases of the rain-induced summer discharge events. The whole bank slid down with the lowering water stage, thus failure was not instantaneous, but evolved as a progressive lowering of failed material down the bank. Note that during the summer discharge events, most often rain caused changes throughout the bank in the beginning of the rising phases of the discharge events.

4.4. Diurnal and seasonal changes in the bank sediment moisture and temperature characteristics

The water content (moisture) and temperature of the sediment varied in different ways at different probe depths at each HOBO sensor location (a-d in Figs. 1–2, 7–9 and Table 4). The sensor, which is located at the top of the bank (location d), recorded the melting of the frozen soil. Its “lower/bottom” probe was installed lying on the still frozen soil layer on 30.5.2017. Note that no more snow was at that location. The temperatures of this probe started rising on 5.6.2017, coincident with the first moisture peak due to the rain (see both “upper/top” and “lower/bottom” moisture probes of the sensor at location d).

Table 10.

The moisture in the loose gravelly sand layers in the HOBO location “c” were the driest of all, as the water had apparently directly flowed through the deeper sediment layers (Figs. 7 and 9, Table 10). However, the porosity here was not possible to measure. The diurnal temperature variation was much greater than in the top sensor location “d”. Thus, the layer at “c” location cooled and warmed much faster than at sensor “d” location on top of the bank.

The principal difference between the response recorded by two sensors (c and d) located high up in the bank versus the two lowest ones (a and b) was that the moisture of the “upper/top probes” at sensor locations a and b were greater than the values of their “lower/bottom probes” (Figs. 1 and 7). This was reversed for sensor locations c and d. The pattern of the moisture change was also different, and indicated that the moisture response of the sensors at locations a and b was not caused by the rain, but rather by water seeping through the bank. In particular the sensor located closest to the toe of the bank (location a) had much greater (c. 0.4 m^3/m^3) moisture content as compared to the other sensors, which had less than 0.3 m^3/m^3 (Fig. 7). The second lowest sensor, i.e. at location b (Figs. 7), showed the moisture development in between the groundwater and precipitation impacts noticed from the sensors at locations a and d. Thus, the differences in the zones of water accumulation and effects were possible to detect.

During the spring melt period (Fig. 8A), the coldest temperatures of the “top / upper” probes at locations a and b occurred during the morning hours, i.e. around 7:00. The temperature of the groundwater area (sensor location a) was clearly warmer on the mornings of 31.5.2017, 2.6.2017, 3.6.2017 and 5.6.2017 than the temperature of the slightly gravelly sand layers at sensor location b. Overall, the difference in the bank sediment temperature data was c. 2–3 °C degrees between the different times of the day. During summer (Fig. 8B), the sensors show that the maximum temperatures occurred in the “upper/top” probes for both locations a and b at around midnight, and the low temperatures at noon. The sensor at location b had greater temperatures throughout that season. Note, that the “lower/bottom” probes at both locations a and b had less diurnal variation during both seasons than the “upper/top” probes had (Fig. 8).

Fig. 7.

Fig. 8.

4.5. Diurnal changes in the surface temperature of the river bank

There is very clear relative difference in surface temperature between the moist groundwater seeping area and the rest of the bank area: the surface temperature of the groundwater area was relatively colder during day, and warmer at night (Fig. 9A: location a). These surface temperature differences were similar to the observations from the diurnal bank sediment temperature variations measured with the HOBO sensor probes (cf. Figs. 7 and 8). Towards the end of the observation period, the relative temperature differences (FLIR camera) had become smaller throughout the bank over the course of the summer (Fig. 10).

The groundwater seeping area was also relatively cooler during the day and warmer during the night/early morning than the surrounding bank surface areas (location 1: Figs. 5, 9 and 10). The loose slightly gravelly sand layers were recognized as the warmest areas also from the FLIR photos (location 2: Figs. 5 and 10). These two distinct areas were the ones most prone to erosion, when the FLIR photos were visually compared to the topographical changes. Thus, groundwater seeping through the bank sediment seems to be the reason for the erosion at the toe in the downstream part of the bank (location 1).

Fig. 9.

By 6.6.2017 (Fig. 10B) all the snow had melted from the bank. The relative temperature differences were less than on 30.5.2017 (Fig. 10A), when patches of snow were still present on top of the bank (right hand side in the Fig. 10A). There were greater temperature differences on 6.9.2017 (Fig. 10C), because the bank surface was drier than in the spring melting period and the sun had heated the bank, especially the driest layers.

Fig. 10.

5. Discussion

The data generated in this study has allowed detection of the temporal evolution of the types of bank failures in a subarctic river. In summary (Fig. 11), the observed erosion was caused by

1) combined rain (short events) and rising water level during the rising phase of the spring snowmelt event (cf. locations 3–5 in Fig. 5). The rain caused changes particularly during the early, rising stages. Water level rises started to influence erosion two days before the discharge peak, when the ground had melted;

2) flowing water during the peak of the spring snowmelt event, complemented by melting of the ground, particularly in the bank toe area (location 2 in Fig. 5);

3) mass failures during the recession phase of the spring snowmelt event (throughout the bank);

4) rain events and related mass failures before the summer high discharge events (throughout the bank, but especially in locations 2–5 in Fig. 5);

5) flowing river water during the peaks of the summer discharge events (toe area);

6) groundwater seeping, continuously after melting of the ground had taken place in spring (location 1 in Fig. 5).

Fig. 11.

All in all, the topographical changes observed during the rising phase of the spring discharge event were less in magnitude and frequency than during the rest of the open-channel flow period. Thus, the erosion during the rising phase of the summer discharge events was greater in magnitude than the erosion during the rising phase of the spring snowmelt discharge event. This indicates that the period of frozen ground is important in modulating the timing of lateral bank erosion. Specifically, fluvial toe erosion started only after the melting of the bank, and was not coincident with the rise of the water level. In 2017, the sediment became unfrozen two days before the spring snowmelt flood peak discharge. Thus, as discussed by Tananaev (2013), the frozen ground limits bank erosion during spring flows, but the melting of the ground (in the case of Pulmanki River especially the melting of the groundwater area) enhances erodibility during low flow open channel periods.

One of the driving agents of the bank failures observed in this study was the impact of flowing river water. The shear forces of the 2017 spring and autumn flows exceeded the critical values for the entrainment of the sediment particles at the bank toe area. The flowing river water had the most impact during the peak discharge period, which lasted two days in early June 2017. The highest number of occurrences of bank erosion events (n=12) observed during the whole study was on the first of two days at which the spring snowmelt discharge peaked. This result is similar to conclusions of Hooke (1979 and 2004), who studied mid-latitude temperate rivers in England, and who highlighted that fluvial erosion is dominantly associated with peak flows.

Secondly, mass failures were also found to be an important cause of topographical changes. For the Pulmanki River, failure events occurred during the recession phases of the flow, causing spatially more extensive and overall greater magnitude of bank recession than the detachment of bank materials by flowing river water alone. But, we note that without the stress caused by flowing water, especially during the peak flood period, no mass failures would have taken place. The erosion was dominantly by shallow planar failures with deposition on the toe. Thus, the bank slumped down based on the gravity and reduced cohesion during the recession phases of the flow. The areas which experienced the greatest erosion were in the toe area consisting of the dry looser sand layers. These could be clearly detected when FLIR photos were analysed against the other measured data during the open-channel period. During the lowering phase of the flood, in addition to the loss of cohesion, the water flow caused stress on the bank toe and transported the collapsed sediment away, further enhancing the mass failure process.

Rain was the third main cause of the bank failures observed in this study. When the frequency of lateral erosion was compared to the moisture sensor data, it was apparent that erosion during the summer period often occurred during rainfall events. Thus, this summertime erosion occurred before the water level of the summer discharge events had risen (Fig. 3 and 6). Small gullies also formed throughout the bank during these rainfall events (cf. locations 3 and 4 in Fig. 5). Thus, during the summer, the rain events caused erosion and deposition to occur more uniformly throughout the bank than during the spring snowmelt period.

The fourth main erosion process noted in this study is associated with the role of groundwater seepage. In particular, low flow seeps, which have previously been reported to act in conjunction with overland flow and fluvial erosion by Fox et al. (2007), also occurred in the Pulmanki River. Fox et al. (2007) note that such low flow seeps are also caused by summer rainstorms. For the Pulmanki River, the bank sediment moisture rose after each rain event and bank collapses occurred after the rain had started and before the rising water level. Our results are also consistent with the observations of Karmaker and Dutta (2013), namely that the total annual river bank erosion in composite river banks can be caused by both groundwater seepage and fluvial erosion. Thus, the results agree with Karmaker and Dutta (2013) and Fox et al. (2007) that erosion was controlled by the combination of groundwater seepage and fluvial erosion, in addition to mass failures.

The present study considered only one bank, which was selected due to its great annual erosion. The bank is complex, with different sedimentary and ground moisture properties down river as well as with height above bed. Thus different processes acted on the bank (groundwater, rain and flowing water) at different locations, and at different times and magnitudes through the season. For example, groundwater seeps were observed only at the downstream end, whereas fluvial toe erosion occurred with the greatest intensity around the apex of the bend during the spring discharge peak, while toe erosion also occurred in the upstream end at the same time. After the flood peak, toe erosion became greater in magnitude in the upstream end of the bend, than around the apex.

The duration of frozen ground on bank erosion has important implications for sediment erosion in an era of climate change. As shorter frozen winter periods have been forecast along with climatic warming in sub-arctic areas (IPCC, 2013), the period of ice protection of river banks will be shorter. In the Pulmanki River, if the bank had not been frozen during the rising 2017 spring snowmelt flood, more frequent and extensive bank erosion would have occurred in the early stages of spring flood. Recent observations of melting ground in Siberia have indicated increased bank and valley slumping in a large arctic river (Séjourné et al., 2015). Therefore, bank erosion processes are expected to become even more important for sediment supply, leading to higher annual sediment yields in (presently) subarctic areas.

For further enhancing our understanding of future climate change impacts on bank erosion processes, studies of wider areas are needed to detect temporal variations in bank erosion processes in other geomorphic and climatic environments and in different types of banks. Frequent topographical measurements using TLS or mobile laser scanning are now fast to employ, and enable rapid data collection for comparison. This study also showed the usefulness of FLIR photos to detect the groundwater seeping areas and the potential areas of erosion within river channels. A further innovation lies in aerial thermal imaging with a sensor capable of saving the temperature values in each pixel. This would enable the detection of the seeping areas from an entire river valley allowing analysis of the connections between thermal properties of the banks, groundwater areas and the sites of lateral erosion.

6. Conclusions

This study provides what is, to our knowledge, the first description of the relative impacts of different driving processes on bank erosion within a full open-channel period in a seasonally frozen, subarctic river. The bank changes occurred in the upstream/inlet, apex and downstream areas of the bend. The magnitude and driving processes varied in these sections with time. The saturated, clayey areas were most prone to erosion caused by continuous seeping of groundwater throughout the open channel flow period.

Bank erosion was least during the rising stages of the spring snowmelt event. The most frequent erosion and deposition at the bank toe took place around the bend apex during the peak snowmelt discharge. Erosion events were slightly more frequent than in the inlet area. However, spatially greater changes in magnitude and number of erosion occurrences were observed during the longer falling phase of the flood and erosion (and deposition) was switched to concentrate in the meander inlet, than in the other sections of the bend.

Rain events and saturation of the bank were the greatest cause of bank changes during the initial stages of the summer discharge events. Erosion was then observed throughout all bank areas. During the falling phases of some summer discharge events, erosion and deposition occurred at the bank toe owing to the loss of cohesion and gravitational slumping.

Overall, mass failures were responsible for more volumetric changes (both at the inlet and the apex) than entrainment at the bank toe by flowing water. However, the processes of fluvial entrainment during the spring and secondary flood peaks, and the loss of cohesion associated with the lowering water level enabled mass failures at these locations. It is also concluded that the changes in elevation and volume were less during the rising phase of the spring snowmelt flood than changes observed in total during the rest of the open channel flow period. Despite erosion events were most numerous at the spring snowmelt discharge peak and its falling stages, greatest total erosion and deposition was during the low flow period after the spring snowmelt discharge event. These results highlight that the spring melt period, while often delivering the largest flows, may not be the main driver of bank erosion in sub-arctic rivers under present climatic conditions. Under fast climatic warming of the arctic and subarctic, the shortening frozen period may induce an earlier and prolonged season of bank erosion in meandering rivers. The interacting processes of seasonal climate and bank erosion described here are important to consider when predicting climate change impacts on the fluvial sedimentary budget.

References

Baker V. R. 1988. Flood erosion. In: Baker VR, Kochel R, Patton P (eds.): Flood geomorphology, 81–95 p. John Wiley and Sons, USA.

Brasington J., James J., Cook S., Cox S., Lotsari E., McColl S., Lehane N. & Williams R., 2016. Catchment-Scale Terrain Modelling with Structure-from-Motion Photogrammetry: a replacement for airborne lidar? Geophysical Research Abstracts Vol. 18, EGU2016-10115-1, 2016 EGU General Assembly 2016.

Burtin A., Hovius N. & Turowski J. M., 2016. Seismic monitoring of torrential and fluvial processes. Earth Surface Dynamics 4: 285–307. DOI: 10.5194/esurf-4-285-2016.

Costard F., Dupeyrat L., Gautier E. & Carey-Gailhardis E., 2003. Fluvial thermal erosion investigations along a rapidly eroding river bank: application to the Lena River (central Siberia). Earth Surface Processes and Landforms 28, 1349–1359.

Darby, S. E. 2005. Refined Hydraulic Geometry Data for British Gravel-Bed Rivers. Journal of Hydraulic Engineering 131, 60–64. DOI: 10.1061/(ASCE)0733-9429(2005)131:1(60).

Demers S., Buffin-Bélanger T. & Roy A. G., 2011. Helical cell motions in a small ice-covered meander river reach. River Res. Appl. 27: 1118–1125. DOI: 10.1002/rra.1451.

Demers S., Buffin-Bélanger T. & Roy A. G., 2013. Macroturbulent coherent structures in an ice-covered river flow using a pulse-coherent acoustic Doppler profiler. Earth Surface Processes and Landforms 38: 937–946. DOI: 10.1002/esp.3334.

Dugdale, S. J., Bergeron N. E., St-Hilaire A., 2013. Temporal variability of thermal refuges and water temperature pattersn in and Atlantic salmon river. Remote Sensing of Environment 136, 358–373. doi: 10.1016/j.rse.2013.05.018.

Fox G. A., Wilson G. V., Simon A., Langendoen E. J., Akay O. & Fuchs J. W., 2007. Measuring streambank erosion due to groundwater seepage: correlation to bank pore water pressure, precipitation and stream stage. Earth Surface Processes and Landforms 32, 1558–1573. DOI: 10.1002/esp.1490

Guo Y. & Shan W. 2011. Monitoring and Experiment on the Effect of Freeze-Thaw on Soil Cutting Slope Stability. Procedia Environmental Sciences 10, 1115 – 1121.

Hazirbaba K., Zhang Y. & Hulsey J. L., 2011. Evaluation of temperature and freeze–thaw effects on excess pore pressure generation of fine-grained soils. Soil Dynamics and Earthquake Engineering 31: 372–384. DOI: 10.1016/j.soildyn.2010.09.006.

Hirvas H., Lagerback R., Mäkinen K., Nenonen K.., Olsen L, Rodhe L. & Thoresen M., 1988. The Nordkalott Project: studies of Quaternary geology in northern Fennoscandia. Boreas 17: 431–437.

Hooke J. M., 1979. An analysis of the processes of river bank erosion. J. of Hydr. 42: 39–62.

Hooke J. M., 2004. Cutoffs galore!: occurrence and causes of multiple cutoffs on a meandering river. Geomorphology 61, 225–238. DOI: 10.1016/j.geomorph.2003.12.006.

Johannson P., 1995. The deglaciation in the eastern part of the Weichsalian ice divide in Finnish Lapland. Geological Survey of Finland, Bulletin 383, 72 pp.

Johansson P., 2007. Late Weichselian deglaciation in Finnish Lapland. Applied Quaternary research in the central part of glaciated terrain. Geological Survey of Finland, Special Paper 46: 47–54.

Julien P. Y., 2002. River mechanics. Cambridge, University Press, 434 pp.

Karmaker T. & Dutta S., 2013. Modeling seepage erosion and bank retreat in a composite river bank. Journal of Hydrology 476, 178 – 187. DOI: 10.1016/j.jhydrol.2012.10.032.

Kasvi E., Laamanen L., Lotsari E. & Alho P. 2017. Flow patterns and morphological changes in a sandy meander bend during a flood – spatially and temporally intensive ADCP measurement approach. Water 9, 106. DOI: 10.3390/w9020106.

Konsoer K. M., Rhoads B. L., Langendoen E. J., Best J. L., Ursic M. E., Abad J. D. & Garcia M. H., 2016. Spatial variability in bank resistance to erosion on a large meandering, mixed bedrock-alluvial river . Geomorphology 252, 80–97. DOI: 10.1016/j.geomorph.2015.08.002.

Kronvang B., Audeta J., Baattrup-Pedersen A., Jensen H. S. & Larsen S. E., 2012. Phosphorus Load to Surface Water from Bank Erosion in a Danish Lowland River Basin. Journal of Environmental Quality 41: 304–313. DOI: 10.2134/jeq2010.0434.

Kämäri M., Alho P., Colpaert A., Lotsari E., 2017. Spatial variation of river ice thickness in a meandering river. Cold Regions Science and Technology 137: 17–29. DOI: 10.1016/j.coldregions.2017.01.009.

Lague D., Brodu N. & Leroux J., 2013. Accurate 3D comparison of complex topography with terrestrial laser scanner: application to the Rangitikei canyon (N-Z). Journal of Photogrammetry and Remote Sensing 82 :10–26. DOI:10.1016/j.isprsjprs.2013.04.009.

Lawler D. M., 2008. Advances in the continuous monitoring of erosion and deposition dynamics: Developments and applications of the new PEEP-3T system. Geomorphology 93: 17–39. DOI: 10.1016/j.geomorph.2006.12.016.

Leyland J., Hackney C. R., Darby S. E., Parsons D. R., Best J. L., Nicholas A. P., Aalto R. & Lague D., 2017. Extreme flood-driven fluvial bank erosion and sediment loads: direct process measurements using integrated Mobile Laser Scanning (MLS) and hydro-acoustic techniques. *Earth Surface Processes and Landforms*, 42, 2, 334–346. Doi: 10.1002/esp.4078.

Leyland .J, Darby S. E., Teruggi L., Rinaldi M., Ostuni D., 2015. A self-limiting bank erosion mechanism? inferringtemporal variations in bank form and skin dragfrom high resolution topographic data. Earth Surface Processes and Landforms 40, 1600–1615. DOI: 10.1002/esp.3739.

Lewis T., Lafreniere M. J., Lamoureux S. F., 2012. Hydrochemical and sedimentary responses of paired High Arctic watersheds to unusual climate and permafrost disturbance, Cape Bounty, Melville Island, Canada. Hydrological Processes 26: 2003–2018. DOI: 10.1002/hyp.8335.

Ling X. Z., Zhang F., Li Q. L., Ana L. S. & Wanga J. H., 2015. Dynamic shear modulus and damping ratio of frozen compacted sand subjected to freeze–thaw cycle under multi-stage cyclic loading. Soil Dynamics and Earthquake Engineering 76, 111–121. DOI: 10.1016/j.soildyn.2015.02.007.

Lininger K. B. & Wohl E., 2019. Floodplain dynamics in North American permafrost regions under a warming climate and implications for organic carbon stocks: A review and synthesis. Earth-Science Reviews 193: 24–44. DOI: 10.1016/ j.earscirev.2019.02.024

Lotsari E., Wang Y., Kaartinen H., Jaakkola A., Kukko A., Vaaja M., Hyyppä H., Hyyppä J. & Alho P., 2015. Gravel transport by ice in a subarctic river from accurate laser scanning. *Geomorphology*, 246: 113–122. DOI: 10.1016/j.geomorph.2015.06.009.

Lotsari E., Wainwright D., Corner G. D., Alho P. & Käyhkö J. 2014a. Surveyed and modelled one-year morphodynamics in the braided lower Tana River. *Hydrological Processes* 28: 2685–2716. DOI: 10.1002/hyp.9750.

Lotsari E., Vaaja M., Flener C., Kaartinen H., Kukko A., Kasvi E., Hyyppä H., Hyyppä J. & Alho P. 2014b. Annual bank and point bar morphodynamics of a meandering river determined by high-accuracy multitemporal laser scanning and flow data. Water Resources Research 50: 5532–5559. DOI: 10.1002/2013WR014106.

Luttenegger J. A. & Hallberg B.R., 1981. Borehole shear test in geotechnical investigations ASTM Spec. Publ., 740, 566-578.

Milliman J. D. & Meade R. H., 1983. World-Wide Delivery of River Sediment to the Oceans. J. Geol. 91, 1–21. DOI: 10.1086/628741.

Neugirg F., Kaiser A., Huber A., Heckmann T., Schindewolf M., Schmidt J., Becht M. & Haas F. 2016. Using terrestrial LiDAR data to analyse morphodynamics on steep unvegetated slopes driven by different geomorphic processes. Catena 142, 269–280. DOI: 10.1016/j.catena.2016.03.021

Qian Y., Mishra D., Tutumluer E. & Kazmee H. A., 2015. Characterization of geogrid reinforced ballast behavior at different levels of degradation through triaxial shear strength test and discrete element modeling. Geotextiles and Geomembranes 43: 393–402. DOI: 10.1016/j.geotexmem.2015.04.012.

Rennie C. D., Millar R. G. & Church M. A., 2002. Measurement of Bed Load Velocity using an Acoustic Doppler Current Profiler. Journal of Hydraulic Engineering 128: 473–483. DOI: 10.1061/(ASCE)0733-9429(2002)128:5(473)

Shen HT. 2010. Mathematical modeling of river ice processes. Cold Reg. Sci. and Tech. 62: 3–13.

Rinaldi M. & Darby S. E. 2008. Modelling river-bank-erosion processes and mass failure mechanisms: progress towards fully coupled simulations. In: Habersack H, Piégay H, Rinaldi M (eds.): Gravel-bed rivers VI: From process understanding to river restoration, 213–239 p. Elsevier B.V.

Rosser N., Williams J., Hardy R. & Brain M., 2017. Insights from high frequency monitoring of coastal cliff erosion. Geophysical Research Abstracts Vol. 19, EGU2017-4749-1, EGU General Assembly 2017, Vienna, Austria, 23–28 April 2017.

Rozo M. G., Nogueira A. C. R. & Castro C. S., 2014. Remote sensing-based analysis of the planform changes in the Upper Amazon River over the period 1986-2006. Journal of South American Earth Sciences 51: 28-44. DOI: 10.1016/j.jsames.2013.12.004.

Séjourné A., Costard F., Fedorov A., Gargani J., Skorve J., Massé M. & Mège D., 2015. Evolution of the banks of thermokarst lakes in Central Yakutia (Central Siberia) due to retrogressive thaw slump activity controlled by insolation. Geomorphology 241, 31–40. DOI: 10.1016/j.geomorph.2015.03.033.

Stroeven, A.P., Hättestrand, C., Kleman, J., Heyman, J., Fabel, D., Fredin, O., Goodfellow, B.W., Harbor, J.M., Jansen, J.D., Olsen, L., Caffee, M.W., Fink, D., Lundqvist, J., Rosqvist, G.C., Strömberg, B. & Jansson, K.N., 2016. Deglaciation of Fennoscandia. Quaternary Science Reviews, 147, 91-121.

Svendsen J. A., Alexanderson H., Astakhovc V. I., Demidov I., Dowdeswell J. A., Funder S., Gataullin V., Henriksen M., Hjort C., Houmark-Nielsen M., Hubbertenk H. W., Ingólfsson O., Jakobsson M., Kjær K. H., Larsen E., Lokrantz H., Lunkka J. P., Lyså A., Mangerud J., Matiouchkov A., Murray A., Möller P., Niessen F., Nikolskaya O., Polyak L., Saarnisto M., Siegert C., Siegert M. J., Spielhagen R. F. & Stein R., 2004. Late Quaternary ice sheet history of northern Eurasia. Quaternary Science Reviews 23: 1229–1271. DOI: 10.1016/j.quascirev.2003.12.008

Tananaev N., 2013. Hysteresis effects of suspended sediment transport in relation to geomorphic conditions and dominant sediment sources in medium and large rivers of Russian Arctic. Hydrology Research. DOI: 10.2166/nh.2013.199

Tananaev N., 2016. Hydrological and sedimentary controls over fluvial thermal erosion, the Lena River, central Yakutia. Geomorphology 253, 524–533.

Thompson C., Croke J., Grove J. & Khanal G., 2013. Spatio-temporal changes in river bank mass failures in the Lockyer Valley, Queensland, Australia. Geomorphology 191, 129–141. DOI: 10.1016/j.geomorph.2013.03.010.

Turcotte B., Morse B., Bergeron M. E. & Roy A. G., 2011. Sediment transport in ice-affected rivers. Journal of Hydrology 409: 561–577. DOI: 10.1016/j.jhydrol.2011.08.009.

Vaaja M., Hyyppä J., Kukko A., Kaartinen H., Hyyppä H., Alho P., 2011. Mapping topography changes and elevation accuracies using a mobile laser scanner. Remote Sensing 3: 5787–600. DOI: 10.3390/rs3030587.

Vandenberghe J., 2001. A typology of Pleistocene cold-based rivers. Quaternary International 79, 111–121.

Walling D. E., 2005. Tracing suspended sediment sources in catchments and river systems. Sci. Total Environ. 344, 159–184.

Walling D. E. & Collins A. L., 2005. Supended sediment sources in British rivers. In: Sediment Budgets 1 (pp 123-133), International Association of Hydrological Sciences Publication No. 291, Wallingford, UK.

Wang J., Sui J. & Karney B. W., 2008. Incipient motion of non-cohesive sediment under ice cover – an experimental study. Journal of Hydrodynamics, Ser. B, 20, 117–124. DOI: 10.1016/S1001-6058(08)60036-0.

Westoby M. J., Brasington J., Glasser N. F., Hambrey M. J. & Reynolds J. M., 2012. 'Structure-from-Motion' photogrammetry: A low-cost, effective tool for geoscience applications. Geomorphology 179: 300–314. DOI: 10.1016/j.geomorph.2012.08.021.

Williams J. G., Rosser N. J., Hardy R. J., Brain M. J. & Afana A. A., 2018. Optimising 4-D surface change detection: an approach for capturing rockfall magnitude–frequency. Earth Surface Dynamics 6: 101–119. DOI: 10.5194/esurf-6-101-2018.

Woo M.-K. & Thorne R., 2003. Streamflow in the Mackenzie Basin, Canada. Arctic 56, 328–340.

Acknowledgements

This work and its field work was supported financially by the Emil Aaltonen Foundation, the Academy of Finland (Extreme and annual fluvial processes in river dynamics [ExRIVER], grant number: 267345; Effects of discharge regulation and erosion control infrastructures on long-term river evolution on cold regions [InfraRiver], grant number: 296090), the Maj and Tor Nessling Foundation (ExRIVER, grant numbers: 201300067 and 201500046), and the Department of Geographical and Historical Studies of the University of Eastern Finland. Funding was also provided by the Strategic Research Council at the Academy of Finland (Competence- Based Growth Through Integrated Disruptive Technologies of 3D Digitalization, Robotics, Geospatial Information and Image Processing/Computing – Point Cloud Ecosystem, grant number: 293389), and the Doctoral Program in Biology, Geography and Geology at the University of Turku.

We would like to thank Linnea Blåfield, Santtu Kaipanen and Markus Katainen from the University of Turku for their valuable fieldwork assistance in 2017. The authors have no conflict of interest to declare.

Appendix 1. The grain sizes based on 2012 measurements

Table 1. The sedimentological characteristics of the study area measured on 13th September 2012. A=toe layer of the bank, B=lower middle layer of the bank, C=middle layer of the bank, D=higher middle layer of the bank. 1= downstream edge of the study area, 9= upstream edge of the study area. Dry sieving was done for the samples, which had mainly coarser than 0.063 mm particles. Coulter counter was done for the portion of the sample, which was smaller than 2 mm. In some samples, no dry sieving was not possible at all due to the large fine particle proportion.

		coordinates (EUREF-FIN)		Dry sieving			Coulter counter		
location	PointID	x	y	D_{10}	D_{50}	D_{90}	D_{10}	D_{50}	D_{90}
down/toe	sedtA1	539615.036	7757291.927	104.73	269.45	980.62	0.92	4.66	12.29
down/toe	sedtA2	539616.942	7757283.296	139.40	300.28	743.23			
down/toe	sedtA3	539616.136	7757276.390	217.39	431.40	835.43			
down/toe	sedtA4	539616.349	7757268.244	82.77	169.12	640.20	7.68	46.10	81.62
down/toe	sedtA5	539614.537	7757260.646	75.01	211.81	751.09			
down/toe	sedtA6	539609.419	7757251.879	246.10	480.70	1085.17			
down/toe	sedtA7	539604.642	7757243.289	109.19	364.28	1150.22			
down/toe	sedtA8	539597.651	7757233.126	100.68	306.93	1414.47	8.62	46.94	76.84
down/toe	sedtA9	539588.335	7757222.919	144.41	463.72	1571.45			
lower middle	sedtB1	539618.908	7757292.682	88.02	195.85	478.05			
lower middle	sedtB2	539621.782	7757283.996	69.07	128.30	195.20	8.37	40.74	73.37
lower middle	sedtB3	539622.411	7757276.268	67.37	126.42	440.66	9.66	44.31	76.25
lower middle	sedtB4	539622.050	7757267.321	75.78	154.98	864.67			
lower middle	sedtB5	539619.325	7757258.977	72.18	160.14	928.76			
lower middle	sedtB6	539614.729	7757248.648	147.00	529.39	1606.21			
lower middle	sedtB7	539609.558	7757240.814				0.89	4.29	11.70
lower middle	sedtB8	539601.979	7757230.565	74.52	196.02	815.59			
lower middle	sedtB9	539594.201	7757219.955				0.87	4.14	11.71
middle	sedtC1	539625.397	7757293.231	88.31	170.77	1779.37			
middle	sedtC2	539627.639	7757283.241	108.86	226.24	351.03			
middle	sedtC3	539627.955	7757275.564				0.90	4.35	11.74
middle	sedtC4	539627.113	7757266.519	104.57	408.86	3096.59	5.45	44.02	76.12

middle	sedtC5	539624.241	7757256.596	114.12	394.24	1734.57			
middle	sedtC6	539619.973	7757245.023	137.40	418.11	995.28			
middle	sedtC7	539614.564	7757235.807	133.86	458.18	1551.63	0.85	4.46	12.46
middle	sedtC8	539606.959	7757226.805	85.00	331.89	1163.84	6.83	44.91	75.15
middle	sedtC9	539600.622	7757214.334	87.96	303.26	751.50			
higher middle	sedtD1	539631.504	7757294.050				25.12	129.30	294.10
higher middle	sedtD2	539634.696	7757282.006	148.18	276.05	342.46			
higher middle	sedtD3	539635.319	7757273.077	121.43	420.74	676.00	9.67	45.41	75.81
higher middle	sedtD4	539634.587	7757265.250	93.83	165.84	854.96	0.92	4.93	12.32
higher middle	sedtD5	539631.621	7757253.025	123.85	392.10	813.31	8.34	49.26	82.05
higher middle	sedtD6	539627.836	7757240.351	133.83	334.06	598.50	34.15	63.90	97.35
higher middle	sedtD7	539621.031	7757230.918	117.07	393.49	1001.83			
higher middle	sedtD8	539613.666	7757221.570	74.85	263.57	682.22	27.97	59.21	89.49
higher middle	sedtD9	539606.441	7757210.350	119.95	358.95	676.72			

Figure captions

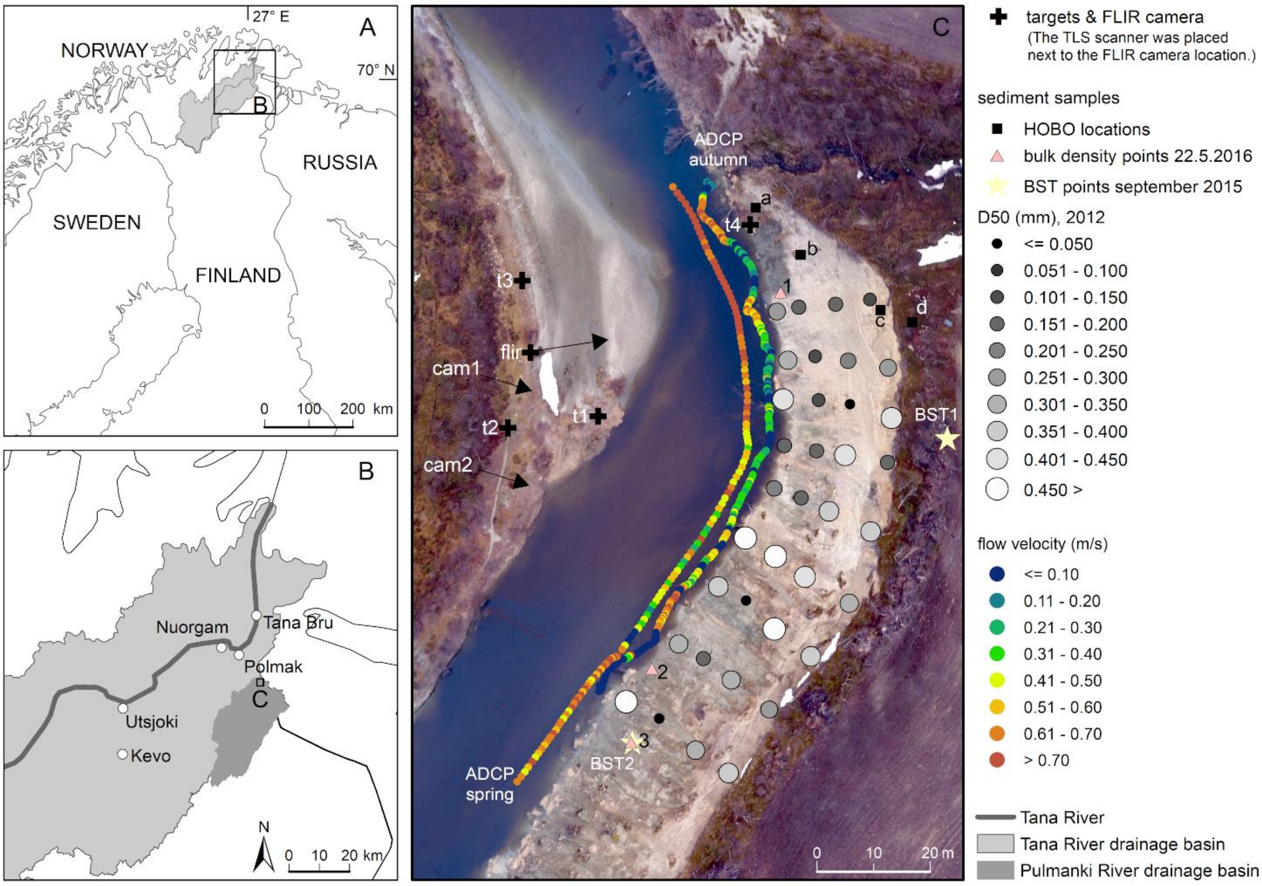

Fig. 1. The study site location, indicating the flow velocities next to the bank (Acoustic Doppler Current Profiler, ADCP: spring 4.6.2017 and autumn 6.9.2017), sediment sample D_{50} values (from 2012 measurements), and the exceedance of the critical velocities for transport (white circles around the toe area's sediment samples). The applied target locations for TLS (t1-t4) are also shown. The time-lapse camera (cam1 and cam2) and FLIR camera locations, and their view directions (arrows) are shown. The locations of the sediment temperature and moisture sensors (i.e. Onset HOBO sensors at a, b, c and d locations, 30.5.-8.9.2017), borehole shear tests (BST1 and BST2, September 2015) and bulk density measurements (numbers 1–3, 22.5.2016) are also illustrated. See the sedimentary data from Tables 5 and 6, and appendix 1. The aerial photo was taken on 3.6.2017.

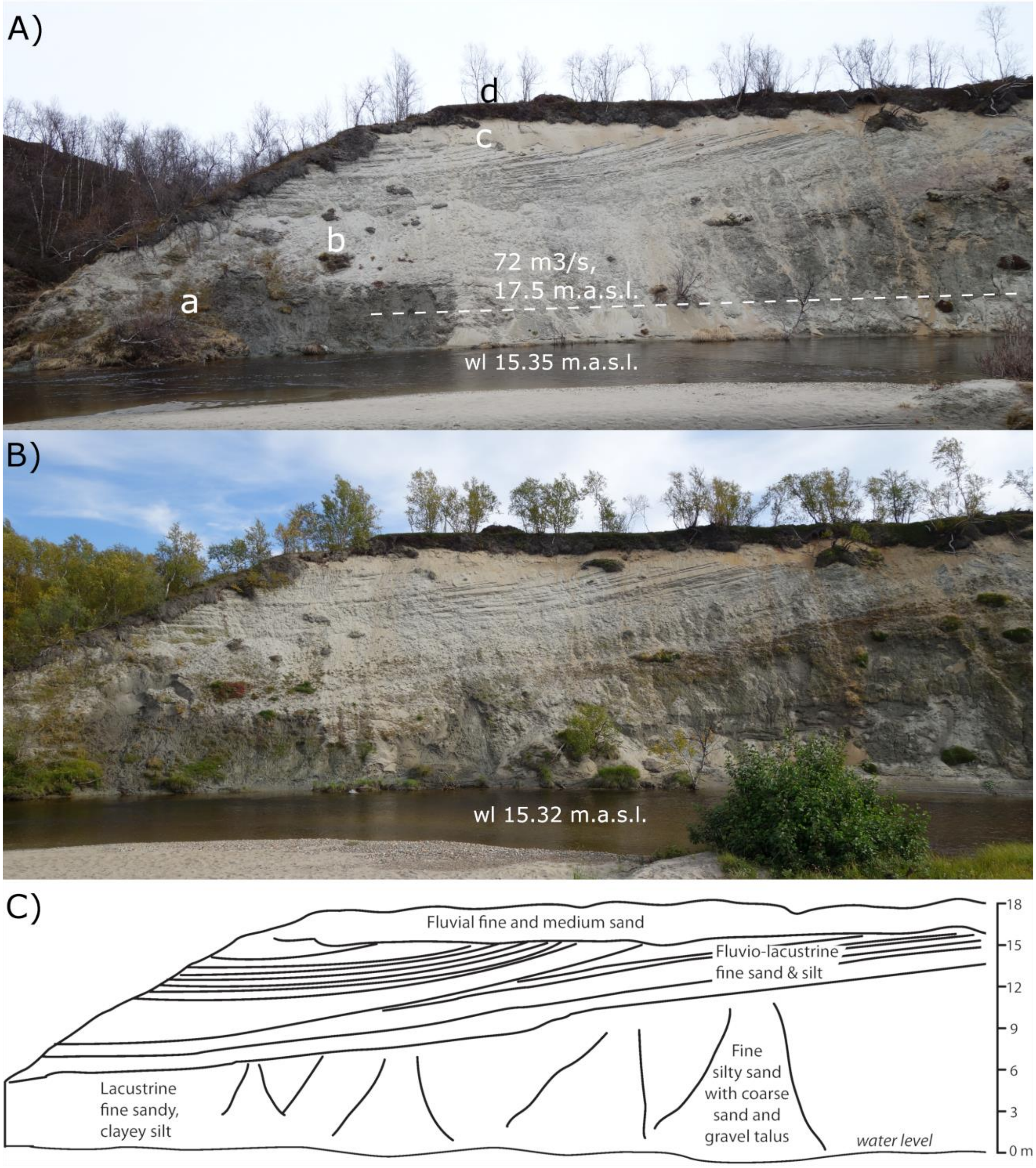

Fig. 2. Seasonal images of the study bank taken with a Sony RX100 camera (photos by Eliisa Lotsari) and illustrating the main stratigraphic units. Flow is from right to left. A) Photo taken in late spring (30.5.2019 at 13:18 GMT+2: discharge c. 9.4 m^3/s; water level 15.35 m.a.s.l., which equals to 0 m in C sub-figure) showing the HOBO sensor locations a-d (cf. Fig. 1), and the peak water level height and discharge of 9.6.2019 (dashed white line); B) Photo taken in early autumn at the end of the open-channel flow period (6.9.2019 at 13:18 GMT+2: water level 15.32 m.a.s.l.); C) The exposed bank shows fluvial, fluvio-lacustrine and lacustrine sediments up to 18 m above water level. Upstream, fluvio-lacustrine sediments give way to horizontally-bedded sand/gravel, and represent fluvial incision and reworking of the older sedimentary units.

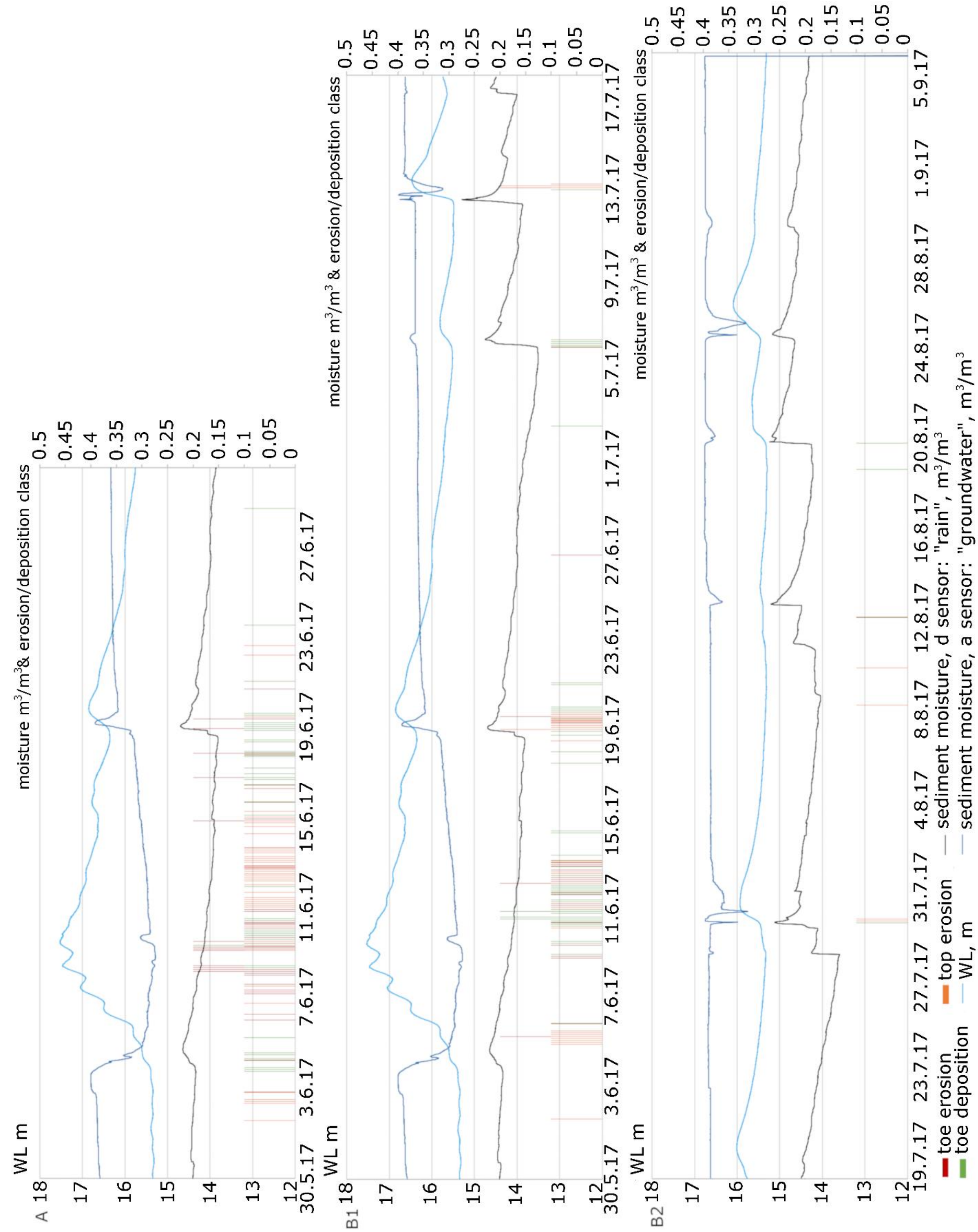

Fig. 3. Overview of water level (m), soil/sediment moisture (m³/m³) and erosion/deposition of bank (qualitative classes 0.1 ["small"] or 0.2 ["great"] classes, without unit) during the study period. The erosion/deposition occurrence is presented from toe, and top section of the bank. A) The occurrence of erosion and deposition at the middle/downstream part of the study area (cam1 data). The camera

filmed from 30.5.2017 until 1.7.2017, when it had ceased working. The upstream part of the study area (cam2 data) is presented in two parts, B1) from 30.5. to 17.7.2017, and B2) from 18.7. to 6.9.2017. Discharge was 10 m^3/s, 72 m^3/s, 13 m^3/s and 4 m^3/s on 3.6.2017 (rising flood), on 9.6.2017 (flood peak), 14.6.2017 (receding phase) and 7.9.2017 (low flow period), respectively. The moisture measured at the top of the bank (see also Fig. 1, sensor location d) reflected the rain events occurring in the area. They clearly show the rain taking place at the beginning of the discharge events.

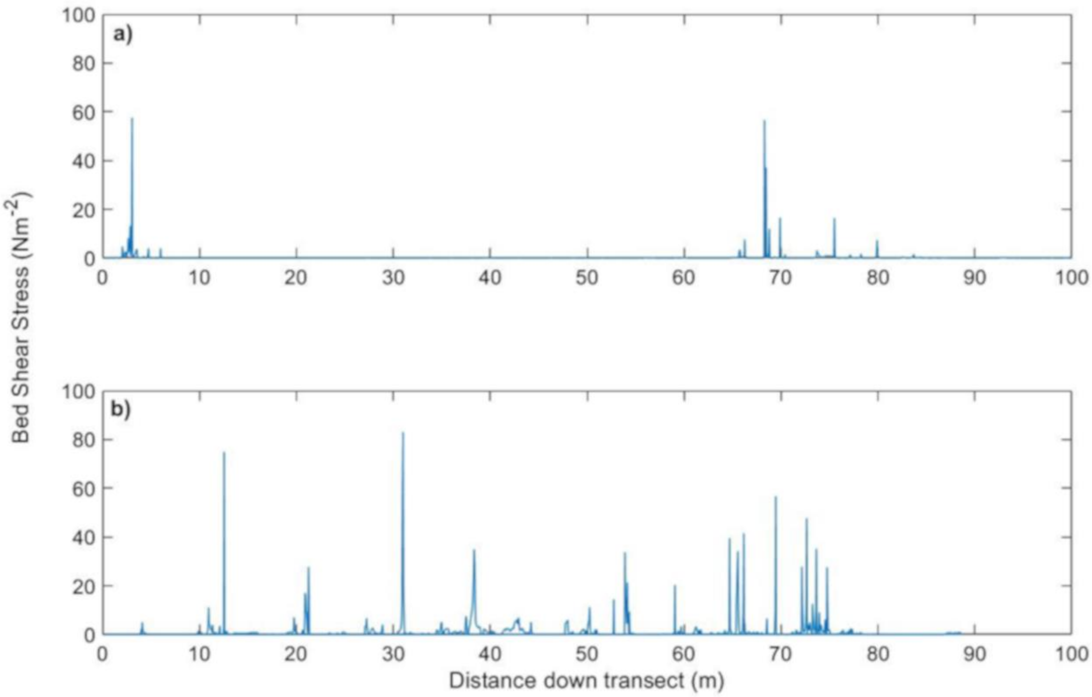

Fig. 4. Bed shear stresses along the bank: a) is the spring data (4.6.2017) and b) is the autumn data (6.9.2017). The x-axis is the distance downstream along the transect (see Fig. 1 and Fig. 5 for transect locations).

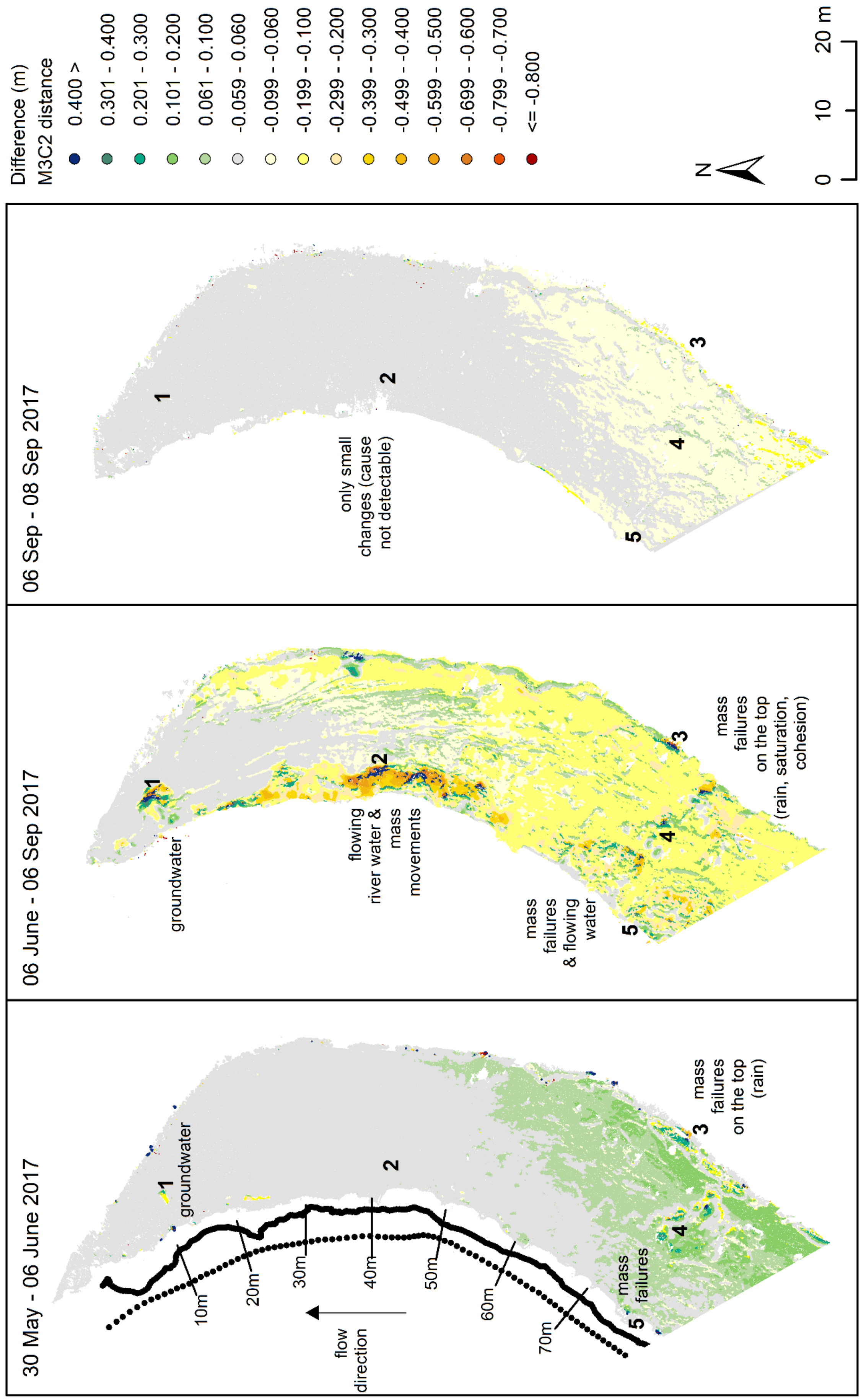
30 May - 06 June 2017
06 June - 06 Sep 2017
06 Sep - 08 Sep 2017
Difference (m)
M3C2 distance
0.400 >
0.301 - 0.400
0.201 - 0.300
0.101 - 0.200
0.061 - 0.100
-0.059 - 0.060
-0.099 - -0.060
-0.199 - -0.100
-0.299 - -0.200
-0.399 - -0.300
-0.499 - -0.400
-0.599 - -0.500
-0.699 - -0.600
-0.799 - -0.700
<= -0.800
N
0
10
20 m
groundwater
mass failures on the top (rain)
mass failures
flow direction
10m
20m
30m
40m
50m
60m
70m
flowing river water & mass movements
mass failures & flowing water
mass failures on the top (rain, saturation, cohesion)
only small changes (cause not detectable)
1
2
3
4
5

Fig. 5. The topographical changes as observed from TLS data. The locations of changes referred to in the text are marked with 1–5, and their values are presented in Table 8. The grey class, i.e. -0.06-0.06 m, is considered as area of “no detectable change”. The ADCP measurement vertical locations (black dots) and the distances from downstream to upstream have been marked on the “30 May 2017–06 June 2017” figure (See the related bed shear stresses from Fig. 4).

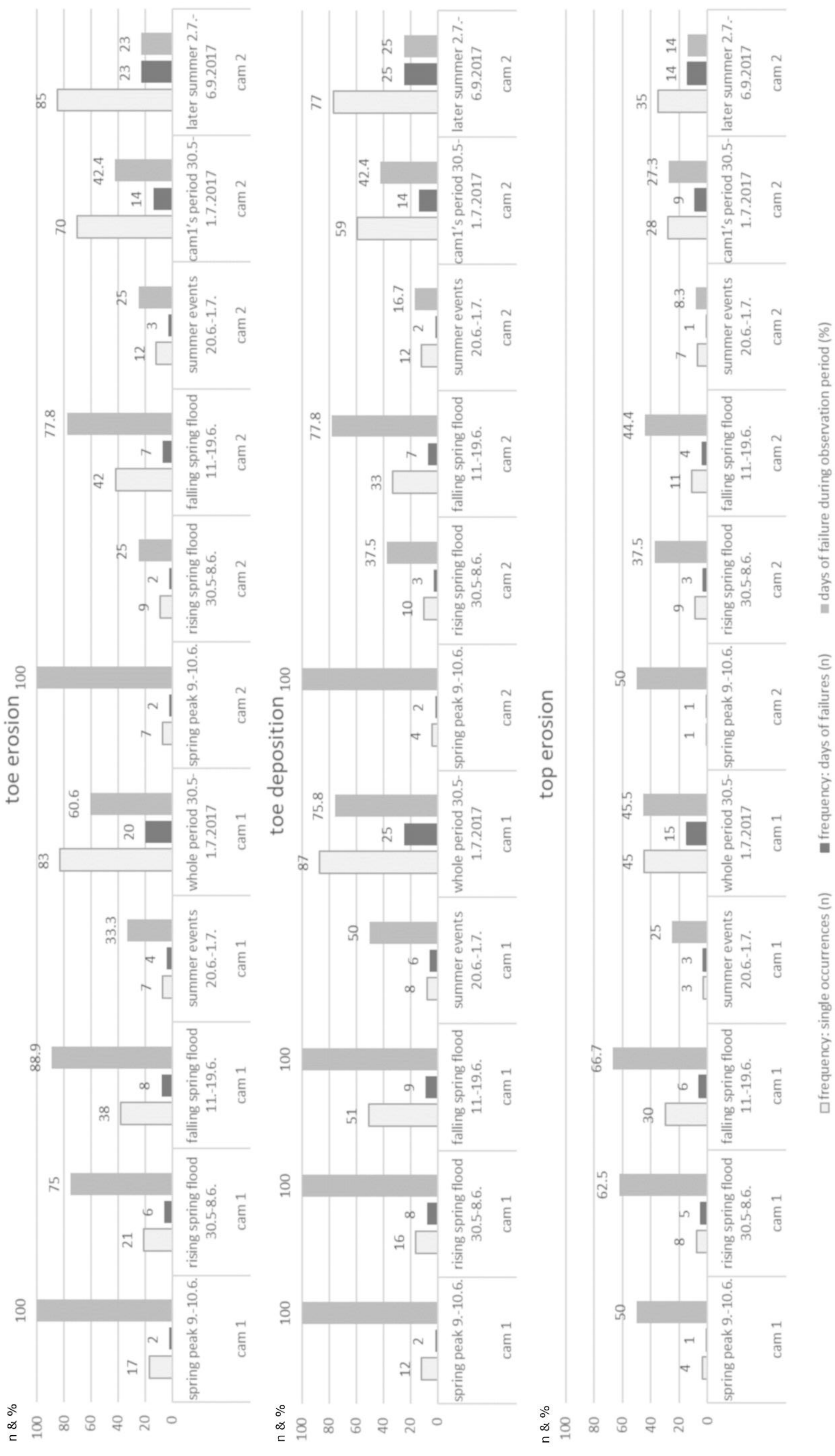
toe erosion
toe deposition
top erosion
n & %
spring peak 9.-10.6.
rising spring flood 30.5-8.6.
falling spring flood 11.-19.6.
summer events 20.6.-1.7.
whole period 30.5-1.7.2017
cam1's period 30.5-1.7.2017
later summer 2.7.-6.9.2017
cam 1
cam 2
frequency: single occurrences (n)
frequency: days of failures (n)
days of failure during observation period (%)

Fig. 6. The frequencies of observed mass failures during different time periods. Bank erosion occurrences were discriminated from the photos of both cam1 and cam2. Note that only cam2 captured changes during the later summer period of 2.7.2017-6.9.2017. The cam1 had ceased functioning on 1.7.2017.

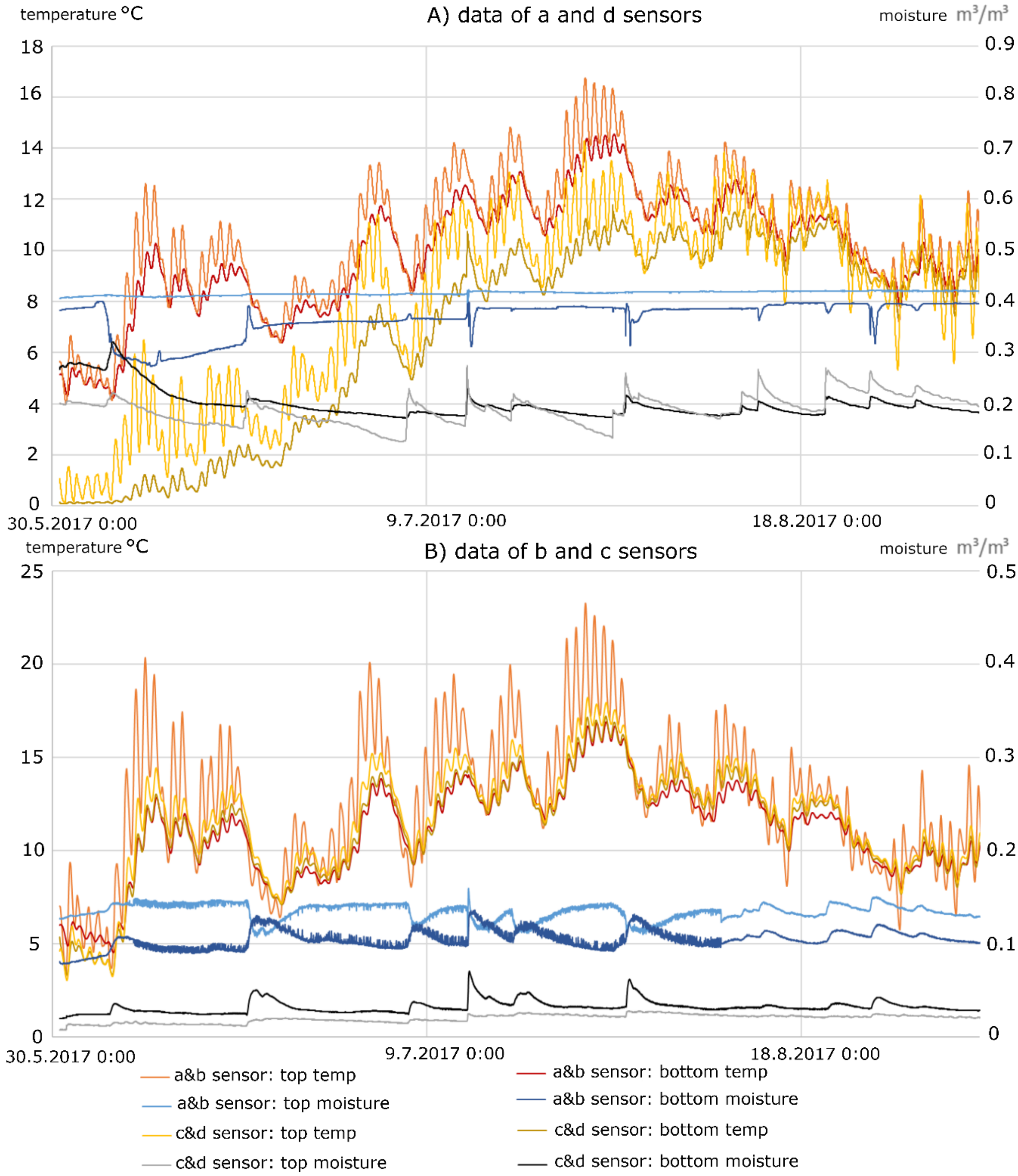

Fig. 7. Variations in bank sediment moisture and temperature from 30.5.2017 to 6.9.2017. Data from the sensors at locations a-d (cf. Fig. 1) are presented. The “top” refers to the “upper probe” and the “bottom” refers to the “lower probe” of each HOBO location (see also Table 4).

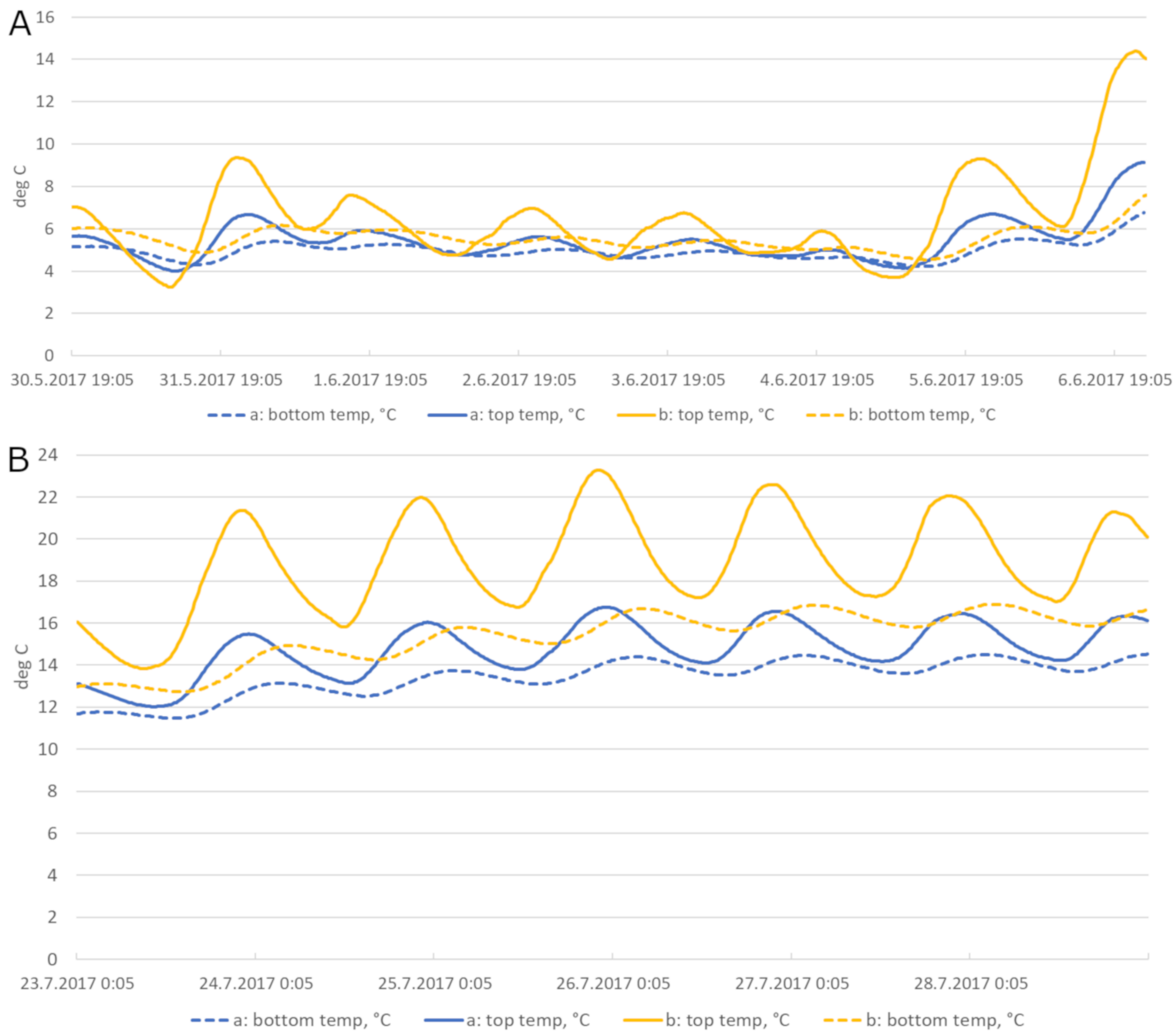

Fig. 8. The temperatures of HOBO sensor locations a (groundwater area) and b (loose sand layers) were selected for more detailed diurnal analyses from A) 30.5.2017-6.6.2017, which is the coolest period presented in Fig. 3, and B) 23.7.2017-28.7.2017, which is the warmest period presented in Fig. 3. groundwater. The “top” refers to the “upper probe” and the “bottom” refers to the “lower probe” of the HOBO sensor locations (cf. Table 4).

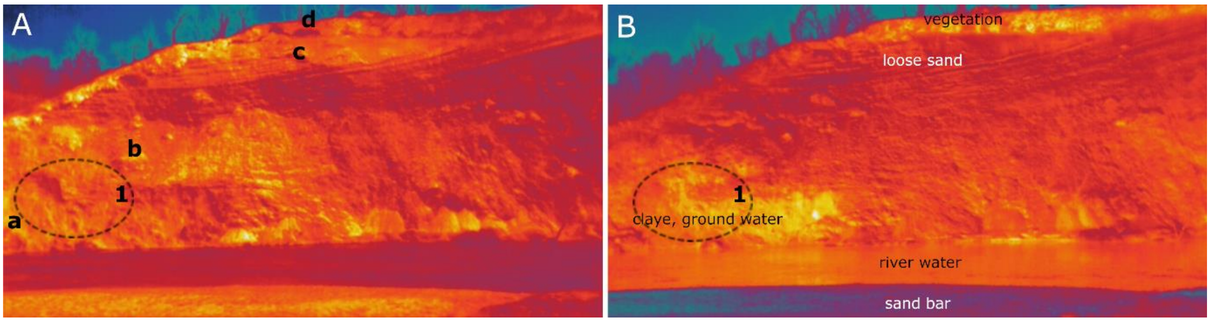

Fig. 9. A) The locations of the HOBO bank sediment moisture and temperature sensors (a–d). On the background a daytime FLIR photo from 1.6.2017 (at 14:19) is superimposed. The more yellow the colour is, the warmer the location is compared to the surroundings. The dry loose sand areas on the top (c), middle (b) and toe areas (in the middle of the figure: no HOBO in those locations) are warm at daytime. The location "a" represents the groundwater area HOBO sensor, and "d" is on top of the bank in the soil layer. B) The night/evening FLIR photo is from 31.5.2017 (at 22:00). The groundwater area is shown as a relatively warmer area (yellow) on the downstream section of the bank, at the bank toe. The erosion area caused by groundwater is roughly presented as a dashed circle (see also this "location 1" from Figs. 5 and 10). Similar conditions occurred at similar times of day during each day of the season in question, but only the best quality images have been selected for display here.

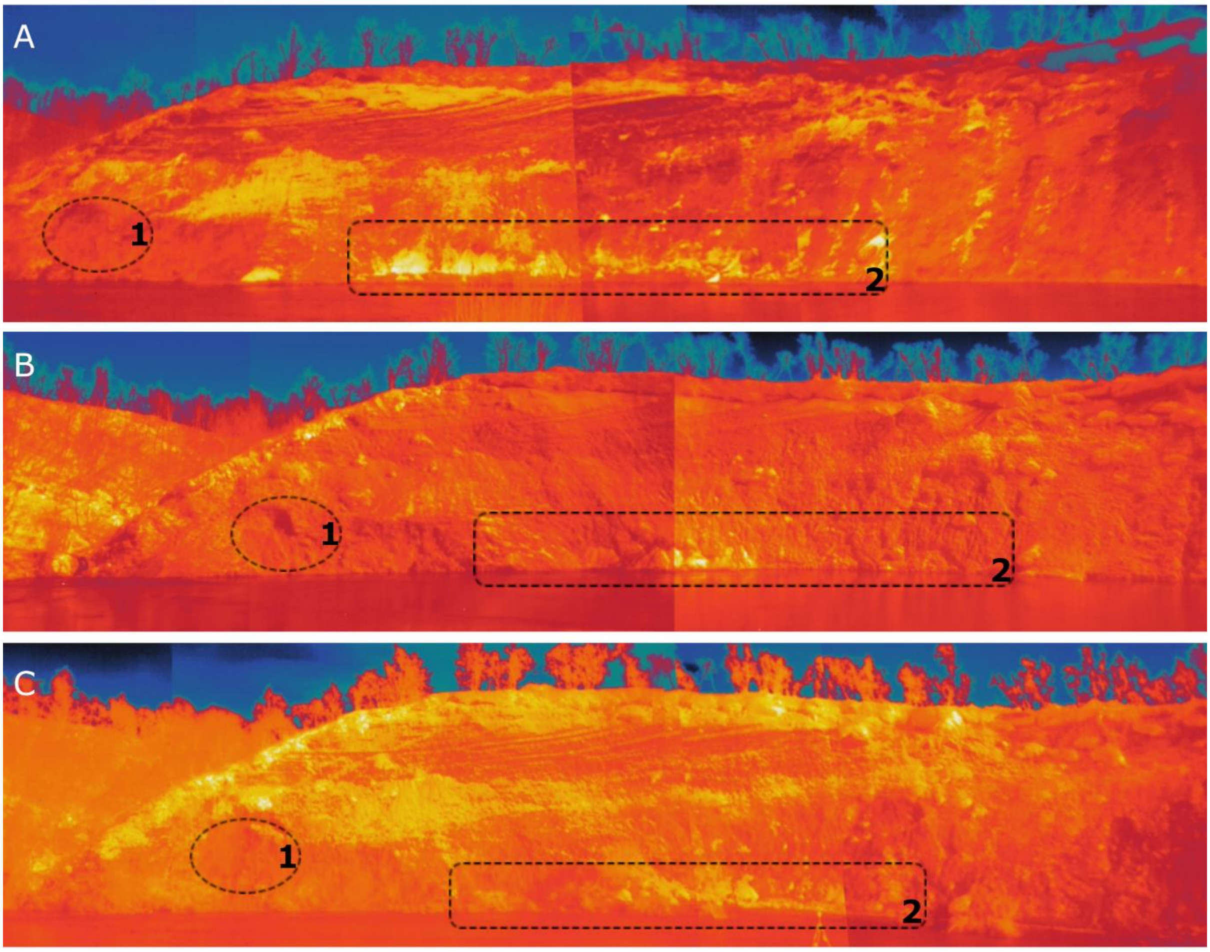

Fig. 10. Daytime FLIR composite photos of the whole study area for three time steps. A) pre-spring flood: on 30.5.2017 at 12:00-12:30. Note that there is snow seen as blue areas on the top of the bank at the right hand side corner of the photo. B) rising stage of spring flood: on 6.6.2017 at 12:30. C) autumn low flow period: on 6.9.2017 at 14:30. The erosion areas caused by groundwater (location 1) and flowing river water (location 2) are roughly presented as a dashed circles (see also the same locations from Fig. 5). The toe erosion location 2 constituted also of loose sand, which is seen in these daytime photos as warmest areas (yellow). Similar conditions occurred at similar times of day during each day of the season in question, but only the best quality images have been selected for display here.

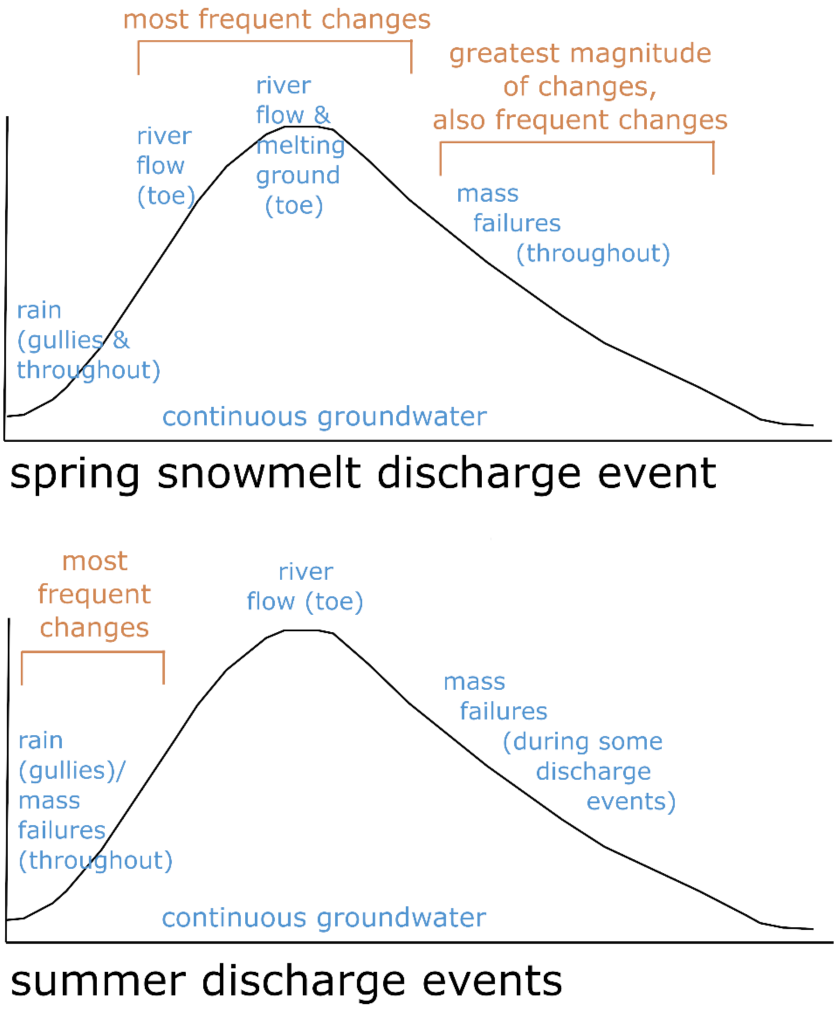

Fig. 11. Conceptual overview of the causes of bank erosion and their timing during spring snowmelt and summer rain-induced discharge events in a subarctic river. The “greatest magnitude” refers to the period with most occurrences of erosion/deposition class 0.2 (great), which are presented in Fig. 3.

Tables

Table 1. The data sets and their measurement specifications.

data set	measurement period	temporal density	Specifications
FLIR photos	30.5.–6.6.2017, 6.–9.9.2017	Every 1 min	Camera showing relative temperatures
RGB photos	12.3.–6.9.2017	Every 2 hours	Two time-lapse cameras (installed next to FLIR)
TLS	30.5.–6.6.2017, 6. and 8.9.2017	Daily	Riegl VZ-400, panorama 10 setting (on 5.6.2017 also second scan with panorama 20 setting)
Bank sediment moisture and temperature	30.5.–6.9.2017	Every 15 min	Onset HOBO microstation sensors.
Water level	30.5.–6.9.2017	Every 15 min	Solinst levelogger, RTK-GNSS
Flow characteristics	4.6.2017 and 6.9. 2017	Long profile	ADCP (Sontek M9 moving platform)
Discharge	31.5.–7.9.2017	Few times in spring and autumn (ADCP), every 15 min (RQ-3, until 16.8.2017 when battery had ended)	ADCP (Sontek M9 moving platform), RQ-30 sensor (Sommer).

Table 2. The accuracies of the georeferencing of the TLS data. The standard deviation of the georeferencing was between 0.006 and 0.030 m. SD=standard deviation. S1= scanning 1, which was measured with panorama 10 settings on 5.6.2017. S2= scanning 2, which is from the same location as S1 on 5.6.2017, but measurement was done with panorama 20 settings.

date of TLS	σ (SD, m)	targets applied (n)	water level (m)
30 May 2017 vs. RTK targets	0.014	3	15.34
31 May 2017 vs. RTK targets	0.009	4	15.32
1 June 2017 vs. RTK targets	0.014	3	15.35
2 June 2017 vs. RTK targets	0.009	4	15.35
3 June 2017 vs. RTK targets	0.006	4	15.35
4 June 2017 vs. RTK targets	0.006	4	15.39
5 June 2017 S1 vs. RTK targets	0.006	4	15.60
5 June 2017 S2 vs. RTK targets	0.006	4	15.60
6 June 2017 vs. RTK targets	0.030	3	15.82
6 September 2017 vs. RTK targets	0.010	3	15.32
8 September 2017 vs. RTK targets	0.018	4	static, no measurement

Table 3. The LoD values between the different scans. The difference/accuracy due to scanner was revealed based on the analyses done between scanning 1 (S1) and 2 (S2) of 5.6.2017. Thus, the scanner itself caused 0.017 m error (italics and bold text). The largest LoD was between 6.6. and 6.9.2017, being 6.2 cm (also bolded).

	68% confidence limit (m)	95% confidence limit (m)
30.5.2017 vs. 31.5.2017	0.016	0.032
31.5.2017 vs. 1.6.2017	0.017	0.032
1.6.2017 vs. 2.6.2017	0.017	0.033
2.6.2017 vs. 3.6.2017	0.011	0.021
3.6.2017 vs. 4.6.2017	0.008	0.016
4.6.2017 vs. 5.6.2017 S1	0.008	0.016
4.6.2017 vs. 5.6.2017 S2	0.008	0.016
5.6.2017 S1 vs. 5.6.2017 S2	0.009	***0.017***
5.6.2017 S2 vs. 6.6.2017	0.031	0.060
5.6.2017 S1 vs. 6.6.2017	0.031	0.060
6.6.2017 vs. 6.9.2017	0.032	**0.062**
6.6.2017 vs. 8.9.2017	0.021	0.041

Table 4. Overview of the locations of the HOBO bank sediment moisture and temperature sensors showing the depths of the “lower/bottom” (moisture + temperature) and “upper/top” (moisture + temperature) probes. The locations (a-d) can be seen on Fig. 1. m.a.s.l.= meters above sea level

HOBO location	bank surface (m.a.s.l.)	lower/bottom probes, depth (m)	upper/top probes, depth (m)	lower/bottom probes (m.a.s.l.)	upper/top probes (m.a.s.l.)	Sediment sample
a: toe	17.64	0.38	0.17	17.26	17.47	clay: not sampled
b: lower middle	20.73	0.42	0.22	20.31	20.51	dry sieved sample (D_{50}=0.193 mm)
c: higher middle	30.66	0.42	0.15	30.24	30.51	dry sieved sample (D_{50}=0.846 mm)
d: top	33.77	0.11	0.04	33.66	33.73	soil layer with roots: not sampled

Table 5. The cohesion parameters and the bulk density data based on borehole shear test analyses.

point names and notes	vertical location within bank	D_{50} (µm)	friction angle (deg)	apparent cohesion (kPa)	bank silt and clay content (% of < 63 µm)
BST1, cf. Fig 1	top	135	35.0	1.5	9.3
BST2, cf. Fig 1	toe	213	36.5	23.5	12.2

Table 6. The bulk densities of Pulmanki River: measurement was done on 22.5.2016 from the bank.

point number	vertical location within bank	bulk density (g/cm³)	D_{50} (µm)
1, cf. Fig. 1	toe	1.43	424
2, cf. Fig. 1	toe	1.50	319
3, cf. Fig. 1	middle	1.73	540

Table 7. The differences between the point clouds calculated with M3C2 tool.

	Significant change			M3C2 distance		
spring dates	valid values (n)	mean (m)	std.dev. (m)	valid values (n)	mean (m)	std.dev. (m)
30.5.-31.5.	224651	0.960	0.195	222793	-0.010	0.040
31.5.-1.6.	333109	0.809	0.393	278807	0.010	0.028
1.6.-2.6.	236486	0.948	0.223	235573	-0.009	0.054
2.6.-3.6.	261794	0.863	0.344	243953	-0.027	0.040
3.6.-4.6.	232629	0.330	0.470	232385	0.002	0.019
4.6.-5.6. S1	265491	0.508	0.500	263900	-0.004	0.034
5.6.S1-6.6.	271054	0.949	0.221	263052	0.076	0.113
longer periods of change						
30.5.-6.6.	224651	0.915	0.280	214429	0.036	0.085
6.6.-6.9.	302105	0.922	0.269	287621	-0.084	0.141
6.9.-8.9.	259459	0.706	0.456	202486	-0.028	0.062

Table 8. The maximum observed erosion and deposition, i.e. distances between the point clouds, at selected locations (cf. Fig. 5).

	spring		summer		autumn	
	erosion (m)	deposition (m)	erosion (m)	deposition (m)	erosion (m)	deposition (m)
location 1	0.16	0.16	0.62	0.60	no change	no change
location 2	no change	no change	0.65 m	no change	no change	no change
location 3	0.46	no change	0.63	0.62	0.14	0.07
location 4	0.32	0.38	0.50	0.50	0.07	0.07
location 5	0.15	0.26	0.40	0.35	0.07-0.08	0.07-0.08

Table 9. The volumetric changes computed between the TLS data sets. The volumetric difference between 5.6.2017-6.6.2017 is uncertain (italics), as these changes were not seen in the M3C2 distance calculations (i.e. elevation difference calculations).

Date	Days between surveys	Volume added (m^3)	Volume removed (m^3)	Volume added per day (m^3/d)	Volume removed per day (m^3/d)	Total volumetric difference (m^3)	Volumetric difference per day (m^3/d)
30.05.-31.05.2017	1	3.0	71.7	2.9	71.7	-68.8	-68.8
31.05.-1.6.2017	1	68.0	4.7	68.0	4.7	63.3	63.3
1.6.-2.6.2017	1	3.2	62.0	3.2	62.0	-58.8	-58.8
2.6.-3.6.2017	1	3.8	140.3	3.8	140.3	-136.5	-136.5
3.6.-4.6.2017	1	18.0	10.2	18.0	10.2	7.8	7.8
4.6.-5.6.2017	1	16.0	20.7	16.0	20.7	-4.7	-4.7
5.6.-6.6.2017	1	452.1	6.0	452.1	6.0	*446.2*	*446.2*
6.6.-6.9.2017	92	11.3	484.2	0.1	5.3	-472.9	-5.1
6.9.-8.9.2017	3	6.7	125.1	2.2	41.7	-118.4	-39.5

Table 10. The sediment properties at the HOBO sensor locations b and c. The material of the bank varied from clay to gravelly sand. The toe location (a) was not possible to analyse with dry sieving, as the material was clay. The top location (d) was not possible to sample, as the sensor was in an organic soil layer with roots.

	lower middle location (b)	higher middle location (c)
D10 (µm)	117	183
D_{50} (µm)	193	846
D_{90} (µm)	353	2761
skewness (arithmetic, µm)	7	2
notes	Unimodal, moderately well sorted	Unimodal, poorly sorted
texture group	slightly gravelly sand	gravelly sand